J. Fluid Mech. (2014), *vol.* 745, *pp.* 409–443.
doi:10.1017/jfm.2014.47

Turbidity currents interacting with three-dimensional seafloor topography

M. M. Nasr-Azadani and E. Meiburg†

Department of Mechanical Engineering, University of California at Santa Barbara, Santa Barbara, CA 93106, USA

(Received 6 March 2013; revised 23 November 2013; accepted 17 January 2014; first published online 21 March 2014)

Direct numerical simulations are employed to investigate the interactions of bidisperse turbidity currents with three-dimensional seafloor topography in the form of Gaussian bumps. Results for two different bump heights are compared against currents propagating over a flat surface. The bump heights are chosen such that the current largely flows over the smaller bump, while it primarily flows around the taller bump. Furthermore, the effects of the settling velocity are investigated by comparing turbidity currents with corresponding compositional gravity currents. The influence of the bottom topography on the front velocity of turbidity currents is seen to be much weaker than the influence of the particle settling velocity. Consistent with earlier work on gravity currents propagating over flat boundaries, the influence of the Reynolds number on the front velocity of currents interacting with three-dimensional bottom topography is found to be small, as long as $Re \geqslant O(1000)$. The lobe-and-cleft structures, on the other hand, exhibit a stronger influence of the Reynolds number. The current/bump interaction deforms the bottom boundary-layer vorticity into traditional horseshoe vortices, with a downwash region in the centre of the wake. At the same time, the vorticity originating in the mixing layer between the current and the ambient interacts with the bump in such a way as to form 'inverted horseshoe vortices', with an upwash region in the wake centre. Additional streamwise vortical structures form as a result of baroclinic vorticity generation. The dependence of the sedimentation rate and streamwise vorticity generation on the height of the bump are discussed, and detailed analyses are presented of the energy budget and bottom wall-shear stress. It is shown that for typical laboratory-scale experiments, the range of parameters explored in the present investigation will not give rise to bedload transport or sediment resuspension. Based on balance arguments for the kinetic and potential energy components, a scaling law is obtained for the maximum bump height over which gravity currents can travel. This scaling law is validated by simulation results, and it provides a criterion for distinguishing between 'short' and 'tall' topographical features. For turbidity currents, this scaling result represents an upper limit. An interesting non-monotonic influence of the bump height is observed on the long-term propagation velocity of the current. On the one hand, the lateral deflection of the current by the bump leads to an effective increase in the current height and its front velocity in the region away from the bump. At the same time, taller bumps result in a more vigorous three-dimensional evolution of the current, accompanied by increased levels of dissipation, which slows the current down. For small bumps, the former mechanism dominates, so that on average the current front

† Email address for correspondence: meiburg@engineering.ucsb.edu

propagates faster than its flat bottom counterpart. For currents interacting with larger bumps, however, the increased dissipation becomes dominant, so that they exhibit a reduced front velocity as compared to currents propagating over flat surfaces.

Key words: gravity currents, stratified flows, topographic effect

1. Introduction

Gravity currents form when a heavier fluid propagates into a lighter, ambient fluid as a result of horizontal hydrostatic pressure gradients (Benjamin 1968; Huppert 1986; Simpson 1997; Borden & Meiburg 2013). Understanding the dynamics of such currents is of general interest, as they occur frequently both in the environment and in engineering applications. Turbidity currents constitute a special class of gravity currents, in which the density difference is caused by suspended sediment. Their flow structure usually gives rise to both erosion and deposition (Kneller & McCaffrey 1999), and hence they represent an important mechanism for the transport of sediment in oceans or lakes (Meiburg & Kneller 2010). Repeated interactions of turbidity currents with the seafloor can result in the formation of a variety of topographical features, among them meandering channels, fans and lobes, gullies, levees, sediment waves and graded bedding (Kuenen & Migliorini 1950; Wynn *et al.* 2000; Migeon *et al.* 2001; Nakajima & Satoh 2001; Normark *et al.* 2002; Wynn & Stow 2002). This renders turbidity currents of interest in the context of hydrocarbon reservoir formation in the deep ocean (Syvitski *et al.* 1996).

Due to the unpredictable and often catastrophic character of natural turbidity currents, many investigations aimed at obtaining insight into their dynamics have employed laboratory experiments, most often involving currents propagating over flat surfaces (e.g. Luthi 1981; Bonnecaze, Huppert & Lister 1993; Gladstone, Phillips & Sparks 1998; de Rooij & Dalziel 2001). Currents over flat substrates are also amenable to simplified theoretical approaches, such as box models, shallow-water models and linear stability analyses (Rottman & Simpson 1983; Bonnecaze *et al.* 1993; Dade & Huppert 1995; Hallworth, Hogg & Huppert 1998; Hall, Meiburg & Kneller 2008; Lesshafft *et al.* 2011). In recent years, fully three-dimensional numerical simulations of turbidity currents propagating over flat beds have become feasible as well (e.g. Necker *et al.* 2002, 2005; Huang, Imran & Pirmez 2008; Cantero *et al.* 2009). Due to their numerical resolution requirements, however, these simulations to date have mostly been limited to laboratory scales. Nevertheless, they have provided detailed information about the dynamics of turbidity currents in simple geometries, including the spatiotemporal evolution of their particle concentration fields, energy budgets, wall-shear stresses and transient statistics.

Comparatively few investigations to date have addressed the dynamics of turbidity currents propagating over more complex seafloor topographies involving slopes or meandering submarine channels (see Woods, Bursik & Kurbatov 1998; Kubo & Nakajima 2002; Kassem & Imran 2004; Kubo 2004; Blanchette *et al.* 2005; Oehy & Schleiss 2007; Peakall *et al.* 2007; Kane *et al.* 2010; Janocko *et al.* 2012; Strauss & Glinsky 2012, and several references cited in Middleton 1993). From these investigations we have gained some insight into the depositional behaviour of turbidity currents (Al Ja Aidi 2000), the nature of their secondary flow in channel bends, and their turbulence structure. However, to the best of the authors' knowledge

a detailed investigation into energy budget components of turbidity currents interacting with three-dimensional seafloor topography has not yet been undertaken. The present investigation aims to provide insight into these issues.

Our knowledge regarding the interaction of constant-density, continuous flows with wall-mounted obstacles is more mature. For example, many experimental and computational investigations have demonstrated the existence of horseshoe vortices, flow separation, vortex shedding and other phenomena in such flow fields (e.g. Baker 1979; Mason & Sykes 1979; Mason & Morton 1987; Belcher & Hunt 1998; Sau *et al.* 2003).

When the flow over obstacles exhibits a stable density stratification, a host of additional phenomena can arise, such as the emergence and breaking of internal waves, the suppression of flow separation, and the formation of hydraulic jumps and internal bores (e.g. Hunt & Snyder 1980; Castro, Snyder & Marsh 1983; Armi 1986; Lin *et al.* 1992; Castro & Snyder 1993; Vosper *et al.* 1999; Eiff & Bonneton 2000; Tseng, Meneveau & Parlange 2006; Ooi, Constantinescu & Weber 2009). Very recently, several investigations have addressed the interaction of compositional gravity currents with spanwise uniform, two-dimensional obstacles (e.g. Gonzalez-Juez, Meiburg & Constantinescu 2009; Tokyay, Constantinescu & Meiburg 2012). Simplified analytical models have been developed that include such features as dividing streamlines and particle pathlines, and that account for internal bores, drag and shear (Snyder *et al.* 1985; Smolarkiewicz & Rotunno 1989, 1990; Gonzalez-Juez *et al.* 2010; Winters & Armi 2012). Many of these investigations have focused on steady or quasisteady flow regimes, whereas the transient interaction of current fronts with obstacles has not been investigated at a comparable level of detail.

The present investigation aims to provide insight into the mechanisms by which turbidity currents interact with three-dimensional seafloor topography. Towards this end, we will focus on the example of a local seamount in the form of a Gaussian bump. We will explore how the topography affects such global properties as the propagation velocity of the current, its sedimentation, the resulting bottom shear stress as well as several other features. In addition, we will analyse the coherent vortical structures of the flow, along with their effect on such quantities as the wall-shear stress and the energy budget. Towards this end, we will employ our computational code TURBINS (Nasr-Azadani & Meiburg 2011; Nasr-Azadani, Hall & Meiburg 2013) to conduct high-resolution, direct numerical simulations of turbidity currents interacting with three-dimensional Gaussian bumps (cf. figure 1). Here, the turbidity currents are generated by the familiar lock–release process. By comparing results for several different bump heights with the flow over a flat surface, we will be able to shed light on how the current/topography interaction mechanisms depend on the bump height. We will present general results regarding the dynamics of compositional gravity currents versus turbidity currents, and concerning the critical bump height, beyond which the current is forced to go *around* the bump rather than *over* it. We furthermore explore currents at different values of the Reynolds number. For a discussion of the resulting deposit profiles, we refer the reader to Nasr-Azadani & Meiburg (2013).

Section 2 formulates the governing equations and the modelling approach, and it describes the flow geometry in detail. Subsequently, we briefly review the numerical approach employed by TURBINS in § 3. Section 4 focuses on such general current properties as the front velocity of turbidity versus gravity currents and the sedimentation rate of the former, and it identifies some non-monotonic dependence on the bump height. Section 5 analyses the vortical structures of the flow,

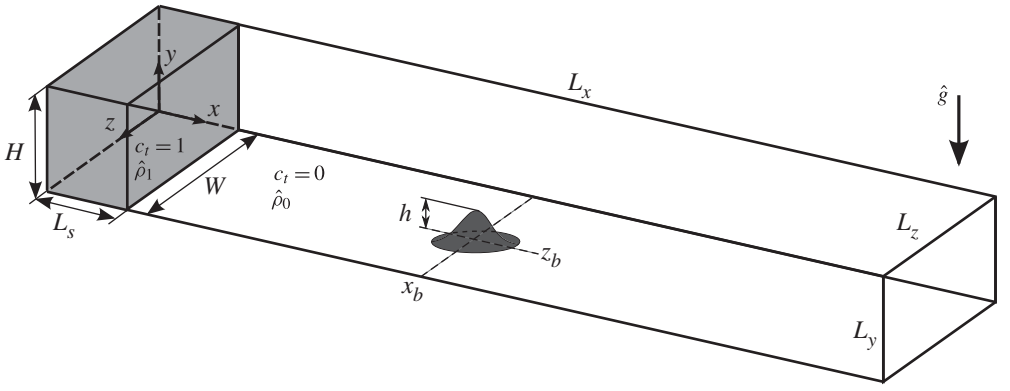

FIGURE 1. Initial set-up for a lock–release turbidity current interacting with three-dimensional seafloor topography in the form of a Gaussian bump. The lock contains a bidisperse suspension. To start the flow, the membrane separating the suspension from the ambient fluid is removed.

and it demonstrates the existence of both traditional and inverted horseshoe vortices. Results for two different Reynolds numbers are compared, with an emphasis on the lobe-and-cleft structures. The section furthermore contrasts currents propagating *over* small bumps with those moving *around* tall bumps, and provides a scaling relationship for the critical current height that separates these two regimes. This scaling law is subsequently validated by analysing the path lines for currents interacting with bumps of different heights. Section 6 provides detailed information on the bottom wall-shear stress, and on the ability of the current to erode the sediment bed. Section 7 focuses on energy budgets, and it identifies some important differences between compositional gravity currents and turbidity currents in this regard. Finally, § 8 employs the detailed information provided by the simulations in order to explain the reasons for the non-monotonic dependence of the long-term front velocity on the bump height observed earlier.

2. Problem description and modelling approach

The modelling approach and governing equations are described in depth by Necker *et al.* (2002) and Nasr-Azadani & Meiburg (2011), so that a brief summary suffices here. We employ the Navier–Stokes equations in the Boussinesq approximation to model dilute suspensions with typical particle volume fractions of $O(1\,\%)$ or less

$$\nabla \cdot \boldsymbol{u} = 0, \tag{2.1}$$

$$\frac{\partial \boldsymbol{u}}{\partial t} + \boldsymbol{u} \cdot \nabla \boldsymbol{u} = -\nabla p + \frac{1}{Re}\nabla^2 \boldsymbol{u} + c_t \boldsymbol{e}^g. \tag{2.2}$$

In the above equations, the non-dimensional quantities $\boldsymbol{u}$, p and c_t represent the fluid velocity, pressure and the total particle concentration (volume fraction), respectively. The Reynolds number Re is defined as

$$Re = \frac{\hat{u}_b \hat{H}/2}{\hat{\nu}}, \tag{2.3}$$

with $\hat{\nu}$, $\hat{H}$ and $\hat{u}_b$ representing the kinematic viscosity, lock height (see figure 1) and buoyancy velocity

$$\hat{u}_b = \sqrt{\frac{\hat{H}}{2}\frac{(\hat{\rho}_p - \hat{\rho}_0)C_r}{\hat{\rho}_0}\hat{g}}, \tag{2.4}$$

respectively. Here, the $\hat{}$ sign refers to a dimensional quantity, whereas symbols without this sign indicate dimensionless quantities. Here C_r, $\hat{\rho}_p$ and $\hat{\rho}_0$ represent, respectively, the initial particle volume fraction within the lock, the density of the particle material and the ambient fluid density. In the above, the half-height of the lock $\hat{H}/2$ and the buoyancy velocity $\hat{u}_b$ serve as characteristic quantities for scaling the flow variables, i.e. $\boldsymbol{x} = \hat{\boldsymbol{x}}/(\hat{H}/2)$, $\boldsymbol{u} = \hat{\boldsymbol{u}}/\hat{u}_b$ and $p = \hat{p}/(\hat{\rho}_0\hat{u}_b^2)$.

By assuming a dilute suspension of small particles, we can neglect particle inertia and particle–particle interactions. Hence, the particles are assumed to move with the fluid velocity plus the Stokes settling velocity

$$\hat{u}_s = \frac{\hat{d}_p^2(\hat{\rho}_p - \hat{\rho})\hat{g}}{18\hat{\mu}}, \tag{2.5}$$

acting in direction of gravity (cf. Dietrich 1982).

The suspension contains two different particle sizes with identical particle material density $\hat{\rho}_p$. For the ith particle size ($i = 1, 2$), we define a continuum concentration field $c_i(\boldsymbol{x}, t)$. Each concentration field is then evolved in an Eulerian manner by

$$\frac{\partial c_i}{\partial t} + (\boldsymbol{u} + u_s^i \boldsymbol{e}^g)\cdot\nabla c_i = \frac{1}{ReSc_i}\nabla^2 c_i, \quad i = 1, 2. \tag{2.6}$$

Here, u_s^i and Sc_i denote the ith particle settling speed and Schmidt number

$$Sc_i = \frac{\hat{\nu}}{\hat{\kappa}_i}, \quad i = 1, 2, \tag{2.7}$$

respectively. In (2.7), $\hat{\kappa}_i$ represents the diffusion coefficient associated with the ith concentration field. Since for $Sc \geqslant O(1)$ the Schmidt number has a negligible effect on the dynamics of the flow (Härtel, Meiburg & Necker 2000*b*), we set all Sc_i to unity. We assign a non-dimensional particle settling speed u_s^i to each particle concentration field, respectively. These values can be translated back into dimensional settling velocities via (2.5). In the present investigation, we employ dimensionless settling velocities of $u_s^1 = 0.03$ (coarse particles) and $u_s^2 = 0.006$ (fine particles), and initial relative mass fractions of 50 % each.

The particle concentration fields C_i are scaled with the total initial volume fraction of the particles in the lock C_r, i.e.

$$c_i = \frac{C_i}{C_r}, \quad i = 1, 2. \tag{2.8}$$

Given the above definition, the total concentration c_t (see (2.2)) at any location can be obtained by adding all of the concentration fields c_i

$$c_t = \sum_{i=1}^{2} c_i. \tag{2.9}$$

Thus, at time $t = 0$, c_t varies between zero in the ambient fluid and one in the lock region.

The computational domain size is $L_x \times L_y \times L_z = 38 \times 2 \times 3$, and the lock has dimensions $L_s \times H \times W = 1 \times 2 \times 3$ (see figure 1). No-slip conditions are imposed everywhere along the boundaries except for the top ($y = L_y$) and side walls ($z = 0, L_z$), where free-slip conditions are employed. To solve for the concentration fields, we implement no-flux boundary conditions at the upstream, downstream, top and side walls, respectively

$$\begin{cases} \dfrac{\partial c_i}{\partial x} = 0 & x = 0, L_x \\ \dfrac{\partial c_i}{\partial z} = 0 & z = 0, \ \ L_z \ \ i = 1, 2. \\ c_i u_s^i + \dfrac{1}{Sc_i Re} \cdot \dfrac{\partial c_i}{\partial y} = 0 & y = L_y \end{cases} \tag{2.10}$$

Along the bottom boundary, we enforce a vanishing normal derivative of the concentration field

$$\boldsymbol{n} \cdot \nabla c_i = 0, \quad y = \Gamma(x, z) \quad i = 1, 2. \tag{2.11}$$

Here, Γ and $\boldsymbol{n}$ denote the bottom surface height and the unit normal vector on the bottom surface pointing toward the fluid region, respectively. We remark that at the bottom, the particles leave the computational domain freely with a constant settling speed u_s^i in the direction of gravity. Moreover, we assume that the deposit layer height is small, so that it does not alter the bottom surface height throughout the simulation. In the current investigation, we do not account for any incipient motion of settled particles in the form of bedload transport and/or erosion and resuspension of particles back into the current (Garcia & Parker 1993; Blanchette *et al.* 2005). In all simulations, the fluid initially is at rest. The particle concentration is set to unity within the lock, and to zero outside. The interface between the suspension and ambient fluid initially is smoothed over three to four grid intervals, in order to avoid any spurious oscillations.

We conduct four main simulations. The first three have identical lock dimensions and suspension properties, but different bottom topographies. Simulation B1 includes a shallow bump, simulation B2 a tall bump and simulation FL a flat bottom for comparison purposes. Furthermore, in order to gain insight into the difference between compositional gravity currents and turbidity currents, we carry out a fourth simulation B2-GC, which is identical to B2 except that the settling velocity is set to zero. Table 1 summarizes the parameter values employed in these simulations. Additional parametric simulations for different bump heights, Reynolds numbers and control volume widths will be referred to in more detail in the relevant sections.

The surface shapes of the bumps in simulations B1, B2 and B2-GC are given by

$$\Gamma(x, z) = h \exp\left(-\frac{(x - x_b)^2 + (z - z_b)^2}{2\epsilon^2}\right). \tag{2.12}$$

The centre of the Gaussian bump is located at $(x_b, z_b) = (5.5, 1.5)$ (see figure 1) and the width parameter ϵ of the bump is set to $\epsilon = 0.25$. The bump height h is 0.25 for B1, and 0.5 for B2 and B2-GC, cf. figure 2.

Name	Shape	Bump height (h)	Re	Number of grid points (N_x, N_y, N_z)	Domain size (L_x, L_y, L_z)	Lock dimensions (L_s, H, W)
FL	Flat	0	2000	(1545, 184, 250)	(38, 2, 3)	(1, 2, 3)
B1	Bump	0.25	2000	(1645, 195, 362)	(38, 2, 3)	(1, 2, 3)
B2	Bump	0.5	2000	(1645, 215, 362)	(38, 2, 3)	(1, 2, 3)
B2-GC	Bump	0.5	2000	(1645, 215, 362)	(38, 2, 3)	(1, 2, 3)

TABLE 1. Parameter sets of the four main simulations.

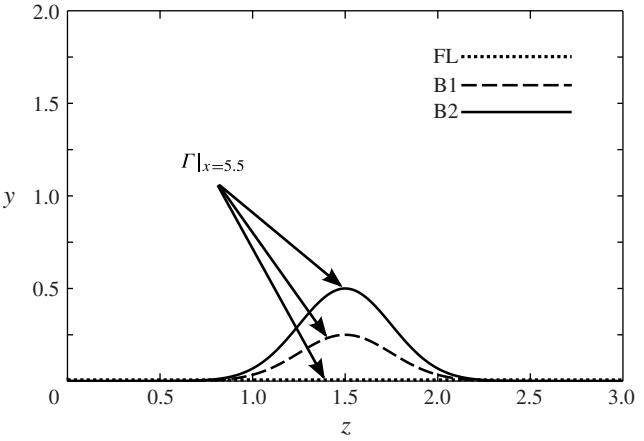

FIGURE 2. Cross-sections of the bottom topography (Γ) in simulations FL, B1 and B2, corresponding to a flat bottom, and bump heights equal to $h = 0.25$ and $h = 0.5$, respectively. The y, z plane is shown at the streamwise location of the bumps peak, $x = 5.5$.

3. Numerical method

Since a detailed description of the numerical method is given by Nasr-Azadani & Meiburg (2011), we provide only a brief summary here. The momentum equations are solved using a projection method (Chorin 1968) in conjunction with the fractional step method (Kim & Moin 1985), on a MAC-staggered grid. We employ a fully implicit central differencing method to discretize the viscous and diffusion terms in the momentum and transport equations, while the convective terms are discretized via an explicit third-order essentially non-oscillatory (ENO) scheme (Harten *et al.* 1987). The time integration for the transport and momentum equations is performed via a second-order total variation diminishing Runge–Kutta method (TVD-RK2; cf. Harten 1997). The boundary conditions along the bottom topography are implemented via an immersed boundary method with direct forcing (Mohd-Yusof 1997; Mittal *et al.* 2008). Validation results, with a focus on accurate wall-shear stress data, are presented in Nasr-Azadani & Meiburg (2011), and comparisons with experiments are described in Nasr-Azadani *et al.* (2013).

We employ a non-uniform structured Cartesian grid in all three directions, cf. figure 3 (Vinokur 1983). In the x direction and in the vicinity of the bump, the grid is uniform with the spacing $\Delta x = 0.0067$. Away from the bump, the grid is smoothly stretched to values $\Delta x = 0.02$ for $0 \leqslant x \leqslant 2$, and to $\Delta x = 0.04$ for $18 \leqslant x$. In the y direction, the minimal spacing $\Delta y = 0.0055$ (B1 $0 \leqslant y \leqslant 0.3$ and B2 and B2-GC

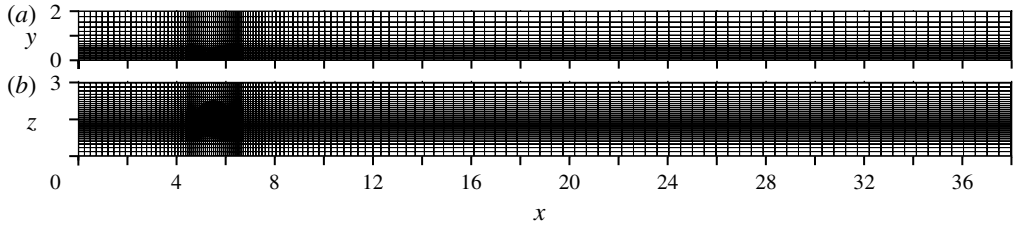

FIGURE 3. Non-uniform structured grid for simulation B2 (see table 1). Every 12th grid point is shown in all directions.

$0 \leqslant y \leqslant 0.55$) is smoothly stretched to the maximum value of $\Delta y = 0.02$ close to the top wall. In the spanwise z direction, a minimum spacing of $\Delta z = 0.0067$ is used in the vicinity of the bump, and stretched to the maximum value of $\Delta z = 0.014$ close to the lateral boundaries.

For case FL, a minimum grid spacing $\Delta x = 0.017$ is utilized close to the lock region, and stretched to $\Delta x = 0.04$ farther downstream ($18 \leqslant x$). A uniform grid is used in the z direction with spacing $\Delta z = 0.012$. In the y direction, the minimal spacing $\Delta y = 0.0055$ ($0 \leqslant y \leqslant 0.1$) is stretched to $\Delta y = 0.02$ close to the top wall.

The above grid spacing ensures that the first grid point above the bottom surface lies within the viscous sublayer. To check this, we define the dimensionless wall-normal distance of this grid point as

$$\eta_n^+ = \frac{\hat{\eta}_n \hat{u}_\tau}{\hat{\nu}} = \eta_n u_\tau Re, \tag{3.1}$$

where $\hat{u}_\tau$ and $\hat{\eta}_n$ represent the friction velocity and wall-normal distance, respectively. In all three simulations we obtain $\eta_n^+ \approx 1$. This allows us to compute the bottom shear stress via linear interpolation from the adjacent velocity grid nodes.

The time integration was generally performed up to $t = 200$, by which the fluid has nearly come to rest in all simulations.

4. General current properties

Here we compare some of the overall current features for the different bottom topographies, such as their suspended mass as a function of time, their sedimentation rates, and their respective front locations. In addition, we will contrast the dynamics of turbidity current B2 with a corresponding compositional gravity current B2-GC.

We define the suspended mass of particle size i as

$$m_s^i(t) = \int_\Omega c_i \, \mathrm{d}V, \quad i = 1, 2, \tag{4.1}$$

with Ω denoting the computational domain. Figure 4 shows the front location x_f of each current, along with the time history of the suspended mass for each particle size. To determine x_f, we average the total concentration c_t in the spanwise and vertical directions, respectively, so that we obtain a one-dimensional profile $c_f(x)$. The front location is then defined as the farthest downstream location at which c_f exceeds the threshold value of 10^{-3}.

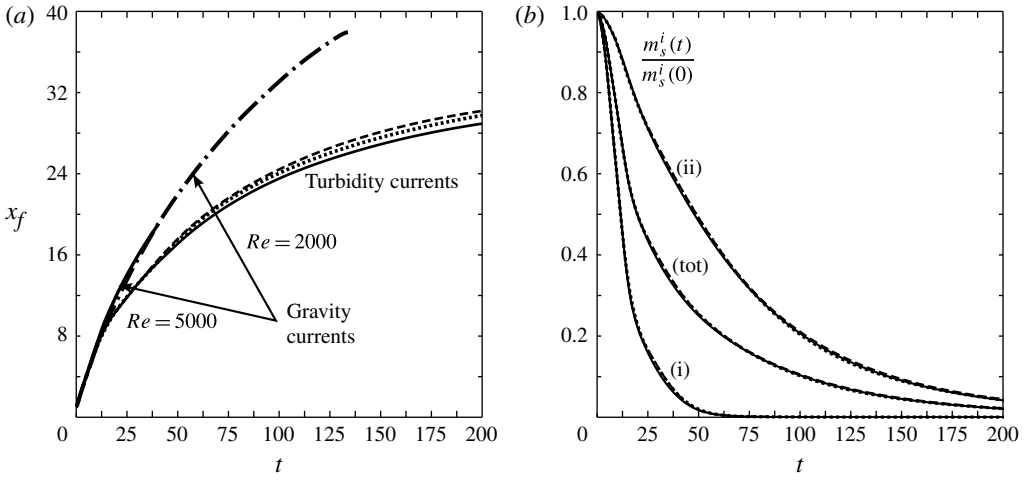

FIGURE 4. Temporal evolution of the front location x_f (*a*) and the suspended mass (*b*). Dots, dashed and solid lines represent turbidity currents FL, B1 and B2, respectively. (i), (ii) and (tot) refer to normalized suspended masses of coarse ($u_s^1 = 0.03$), fine ($u_s^2 = 0.006$) and all particles, respectively. The bump height has a non-monotonic influence on the front location, in that B1 advances faster than FL, whereas B2 propagates more slowly than FL and B1. The front location of the compositional gravity current B2-GC at $Re = 2000$ is shown for comparison (dash-dotted line), along with the front location of a simulation identical to B2-GC except that $Re = 5000$ (solid line). The Reynolds number has a negligible effect on the front velocity. The bottom topography is seen to have only a weak influence on the rate at which the suspended mass decreases with time.

We observe that after a brief initial transient all currents propagate with nearly the same constant velocity. During this stage of the current, which includes the well-studied slumping phase (Huppert & Simpson 1980), the front velocity of the current is largely independent of the settling velocity. After $t \approx 15$, all three turbidity currents gradually slow down in comparison with the compositional gravity currents, since they increasingly lose suspended particles, so that their driving force diminishes. For all of the turbidity currents, at $t = 20$ only $\sim 50\,\%$ of the particle mass is still in suspension. While the presence of the obstacles does not have a significant influence on the mass of the suspended particles, the front location of the turbidity currents displays an interesting non-monotonic behaviour: current B1 over the small bump moves faster than current FL over the flat substrate; however, a further increase in the bump height to B2 results in a current that is slower than both B1 and FL. We will further explore the reasons for this non-monotonic behaviour below, in the context of discussing the effective current heights and dissipation rates for each of the currents.

Figure 5 shows the time history of the sedimentation rate on the bottom surface $\dot{m}_d(t)$, defined as the time derivative of the suspended particle mass. For each particle size

$$\dot{m}_d^i = -\int_A u_s^i c_w^i \boldsymbol{e}^g \cdot \boldsymbol{n}\, \mathrm{d}A, \quad i = 1, 2. \tag{4.2}$$

Here, c_w denotes the particle concentration at the bottom wall, and A represents the bottom surface area.

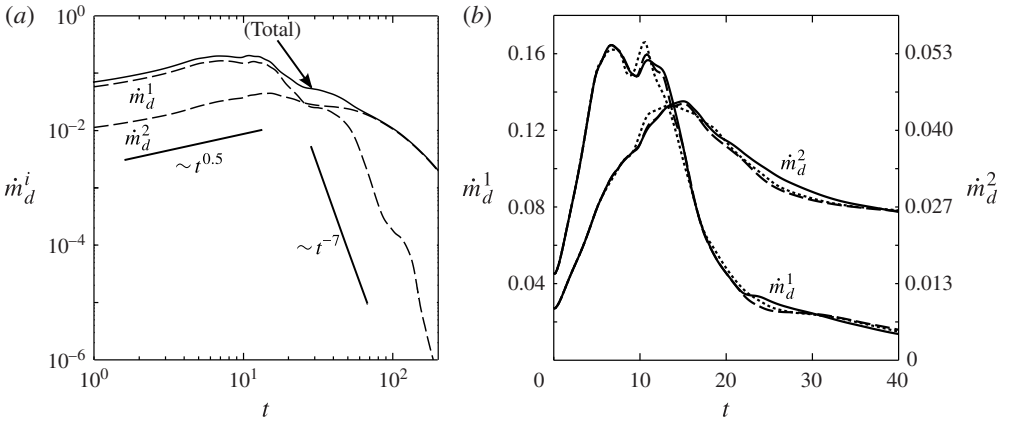

FIGURE 5. Time history of particle sedimentation rate for coarse ($\dot{m}_d^1$) and fine ($\dot{m}_d^2$) particles. (*a*) Case B1 shown on a logarithmic scale. (*b*) Comparison of all cases, where dotted, dashed and solid lines represent cases FL, B1 and B2, respectively.

Both particle sizes experience two distinctly different stages. During the first stage, the sedimentation rate can be approximated by a power law in the form of $\dot{m}_d^i(t) \sim t^{0.5}$. This is consistent with the observation by Necker *et al.* (2002) for a monodisperse current with a particle settling speed of $u_s = 0.02$ propagating over a flat wall. Equation (4.2) indicates that, for a current with constant concentration along the bottom wall, the sedimentation rate would be proportional to the bottom surface area covered by the current. Since the front velocity is nearly constant during the early stage, this would result in a linear increase of the sedimentation rate with time. Hence, the observed exponent of 0.5 must be due to variations in the particle concentration along the bottom surface as a result of mixing, or as a result of the bore that is reflected from the back wall of the lock region.

Figure 6 verifies the above picture for the early stages of the flow. On the one hand, the particle concentration at the bottom wall is reduced in the vicinity of the nose region due to the thin layer of ambient fluid that is overrun by the current front as a result of the no-slip condition at the bottom wall. In addition, as the bore reflected from the left wall propagates forward, it reduces the particle concentration at the wall in the tail section of the current. Hence, for longer or deeply submerged locks, or for slip conditions along the bottom wall, we would expect to see a different dependence of the sedimentation rate on time (Necker *et al.* 2005).

After $t \approx 15$, the turbidity currents undergo the aforementioned deceleration. We note that this time corresponds approximately to the peak sedimentation rate. In addition to losing suspended particles, the currents are being diluted as ambient fluid is entrained via turbulent mixing. This phase coincides with a dramatic change in the sedimentation rate for both particle sizes. The rate at which the coarse particles sediment out decreases rapidly, following a power-law exponent of approximately $n = -7$. This compares with a value of $n = -2.4$ observed by Necker *et al.* (2002) for a monodisperse current with $u_s = 0.02$, which suggests that the sedimentation rate during the deceleration phase is a function of the particle settling speed. Furthermore, we note that the nonlinear coupling between different particle sizes will also influence the temporal decay of the sedimentation rate, as discussed by Gladstone *et al.* (1998) and Harris, Hogg & Huppert (2002).

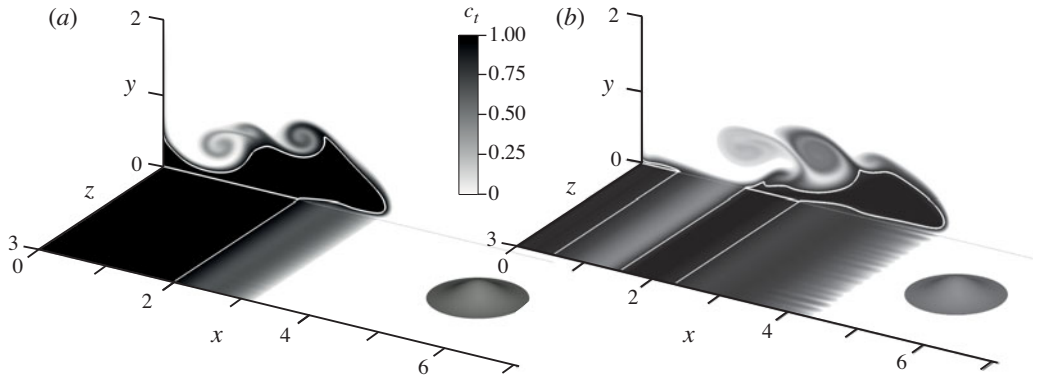

FIGURE 6. Temporal evolution of the concentration (c_t) along the bottom wall during the initial sedimentation phase for case B1: (*a*) $t = 4$; (*b*) $t = 6$. The vertical plane depicts the concentration profile in the centreplane $z = 1.5$. The white lines represent the $c_t = 0.95$ contour. We find that the particle concentration at the bottom wall is reduced by the thin layer of ambient fluid overrun by the current front, and by the bore reflected from the back wall of the lock.

For fine particles, on the other hand, the sedimentation rate does not follow a power law during this phase. Beyond $t = 50$ nearly all of the coarse particles have settled out, so that the total sedimentation rate follows that of the fine particles. Figure 5(*b*) compares the respective sedimentation rates for the FL, B1 and B2 cases. We find that the bottom topography has a very weak influence on the rate at which the particles settle out.

Figure 7 compares the current heights of flows B2 and B2-GC at different times. To compute the current height, we integrate the spanwise averaged concentration field in the y direction. We note that a variety of current height measures have been employed in the past, such as the current moment (cf. Ellison & Turner 1959), the half-height of the lock (cf. Shin, Dalziel & Linden 2004) and the depth-integrated density profile (cf. Birman, Martin & Meiburg 2005). Upon arrival of the current at the bump location, both cases demonstrate very similar current height profiles. Beyond this stage, however, the turbidity current experiences a more pronounced deceleration, while the frontal region of the compositional gravity current maintains a thicker profile, which accounts for its larger sustained front velocity.

In summary, we find that the influence of bottom topography on the front velocity of turbidity currents is much weaker than the influence of the particle settling velocity. The effect of the bump height on the current velocity is non-monotonic, so that the current interacting with a bump of intermediate height advances more rapidly than its counterparts propagating over a flat bottom or interacting with a tall bump. All turbidity currents begin to decelerate appreciably sometime after having interacted with the bump. A corresponding compositional gravity current, on the other hand, is able to maintain a substantially higher front velocity for longer times.

5. Structure of the current

The erosional and depositional nature of turbidity currents is dominated by their large-scale vortices. Hence, in this section we focus on characterizing these vortical structures, and on how their evolution is affected by the bottom topography. We

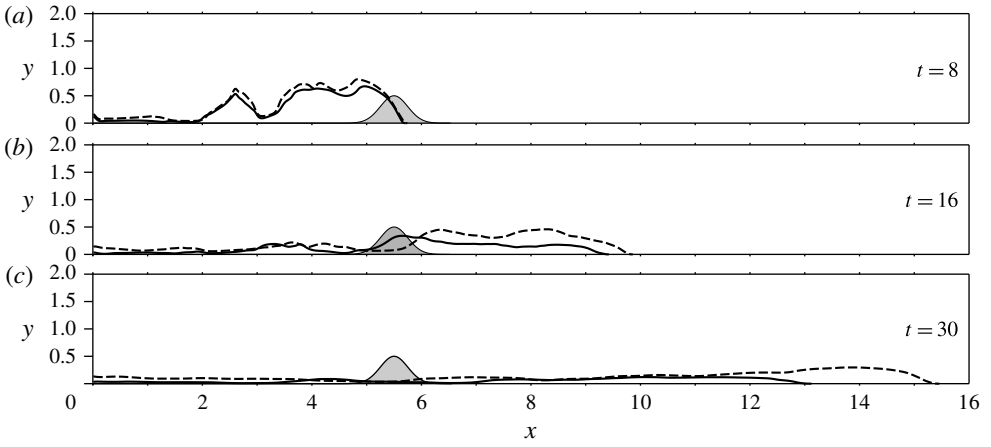

FIGURE 7. Current height for cases B2 (solid line) and B2-GC (dashed line), at three different times. After interacting with the bump, the front of the compositional gravity current B2-GC maintains a larger height and thus travels faster.

furthermore compare currents propagating *over* small bumps with those flowing *around* larger bumps, and we derive scaling arguments for the critical bump height that separates these two parameter regimes. We subsequently validate this scaling law by analysing particle path lines for currents interacting with bumps of different heights. We furthermore compare the vortical and lobe-and-cleft structures for currents of two different Reynolds numbers, and we assess the influence of the lateral domain boundaries by contrasting two simulations for different computational domain widths.

Figure 8 illustrates the temporal evolution of turbidity current B1 by visualizing the $c = 0.1$ contours of the coarse and fine particle concentration fields, respectively. During the initial phase, the flow is dominated by a pair of spanwise startup vortices (Härtel *et al.* 2000*b*), although a noticeable lobe-and-cleft instability is emerging after $t = 6$. Around $t = 8$, the current head encounters the obstacle and experiences some lateral deflection. We note that, during these early stages, the concentration fields of the coarse and fine particles are quite similar. Over long times, however, we expect the different settling velocities of the coarse and fine particles to result in major discrepancies. This is confirmed by the frames for $t = 16$, which show that many of the coarse particles have already settled out, while most of the fine particles remain in suspension.

Figure 9 compares the structure of the B1 and B2 currents as they encounter the obstacle, with the FL current at the same time. While the front of FL is dominated by the lobe-and-cleft instability (Simpson 1972; Härtel, Carlsson & Thunblom 2000*a*), B1 and B2 are noticeably influenced by the obstacle. However, while B1 primarily *passes over* the bump, the front of B2 is bisected by the bump, so that it mostly *flows around* it. Hence, at $t = 12$, the front of B1 resembles the FL case again, while B2 still exhibits a strong wake effect.

The different front dynamics of B1 and B2 are clearly visible in figure 10, which shows the concentration field in the plane $x = 5.5$, along with the v- and w-velocity components, for times 8 and 12. During the impact stage at $t = 8$, the front of B1 is seen to flow over the bump, while the taller bump in case B2 bisects the front, deflecting it laterally away from the highest point. The ambient fluid above both

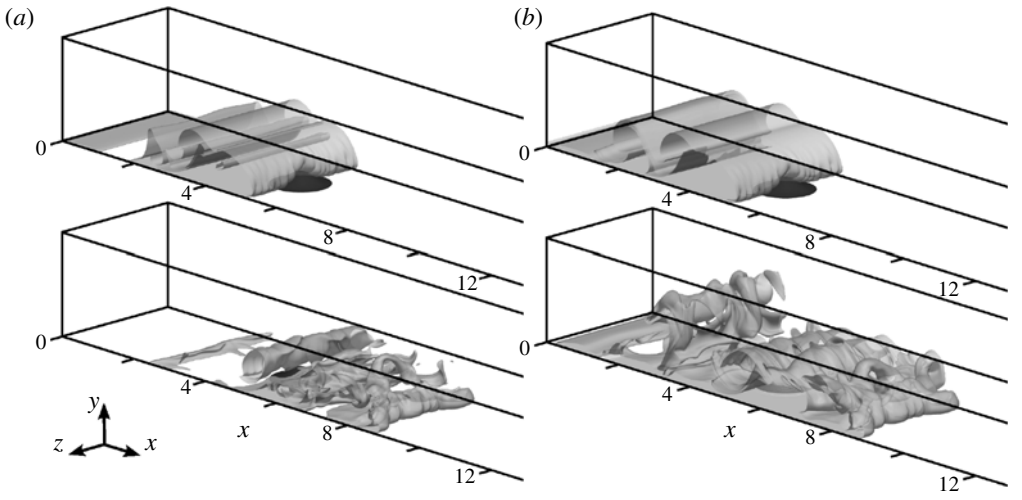

FIGURE 8. Temporal evolution of the turbidity current produced by a lock release flow passing over a Gaussian bump (case B1). The $c = 0.1$ isosurfaces of the particle concentration fields are shown for the coarse (*a*) and fine particles (*b*), respectively. From top to bottom, times are 8 and 16.

currents is deflected upwards at this time. Both fronts exhibit plumes of the lighter, ambient fluid from the overrun boundary layer rising upward from the bottom wall, as a result of the lobe-and-cleft instability. At $t = 12$, both currents plunge downward in the plane $x = 5.5$; however, B2 maintains a bisected front.

The above discussion raises the general question about the limiting bump height that the current is able to travel over, and beyond which it will have to go around the bump. For linearly stratified flows over obstacles, issues such as the existence of dividing streamline, the generation of internal waves and vortex shedding have been the focus of several investigations (Snyder *et al.* 1985; Smolarkiewicz & Rotunno 1990; Winters & Armi 2012). However, we are not aware of corresponding investigations for transient current fronts interacting with obstacles.

In the following, we first consider currents with vanishing settling velocities, in order to develop scaling arguments that are independent of this quantity. Due to the relatively high Reynolds numbers and low dissipation rates of the gravity currents under investigation, we can follow the analysis by Snyder, Britter & Hunt (1979), and employ balance arguments for the kinetic and potential energy components in order to assess the currents' capacity to travel *over* an obstacle of a given height. Those authors argue that a heavier fluid layer of thickness $\hat{h}_c$ submerged below a lighter ambient fluid of density ρ_0 can flow over a hill of height $\hat{h}_b$ if

$$\frac{\hat{U}_\infty^2}{\hat{g}\hat{h}_c\Delta\hat{\rho}/\hat{\rho}_0} > 2\left(\frac{\hat{h}_b}{\hat{h}_c} - 1\right) \tag{5.1}$$

is satisfied, where $\Delta\hat{\rho}$ denotes the density difference. Here, $\hat{U}_\infty$ represents the upstream velocity of the dense current. Employing the reference variables of the present study, (5.1) can be written in dimensionless form as

$$\frac{U_\infty^2}{h_c} = 2\left(\frac{h_b}{h_c} - 1\right). \tag{5.2}$$

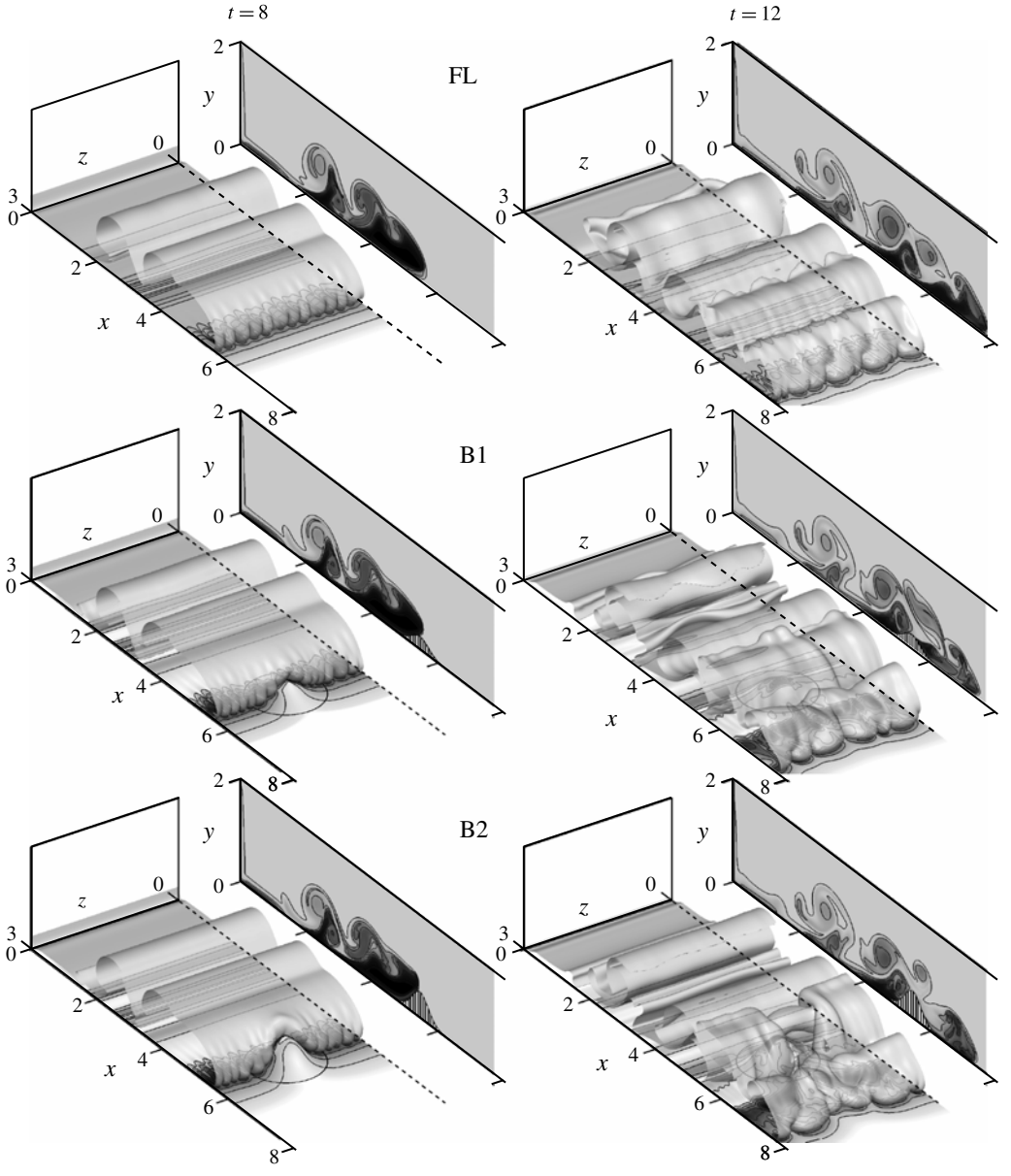

FIGURE 9. Development of the current structure for cases FL, B1 and B2, visualized by the concentration contour $c_t = 0.1$. FL is dominated by the growth of lobe-and-cleft structures in the frontal region, whereas cases B1 and B2 show a strong influence of the bump. While current B1 primarily flows *over* the shallow bump, current B2 mostly flows *around* the taller bump. The shading in the bottom plane indicates the magnitude of the wall-shear stress, and the vertical plane to the right depicts the concentration field in the symmetry plane $z = 1.5$.

Upon arrival of the current at the bump location ($t \approx 10$), the front velocity is approximately $U_\infty \approx 0.7$, with a current height $h_c \approx 0.7$. Equation (5.2) then suggests

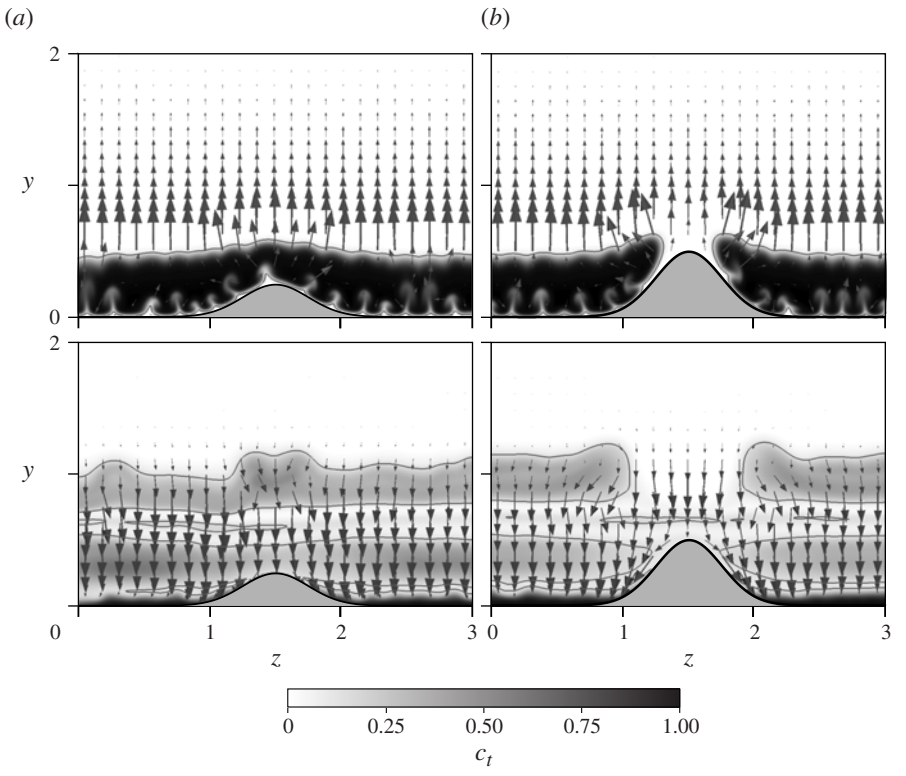

FIGURE 10. Evolution of currents (*a*) B1 and (*b*) B2 in the plane of the peak of the bump at $x = 5.5$. The top row corresponds to $t = 8$, whereas the bottom row depicts the currents for $t = 12$. The in-plane v, w-velocity vectors are also shown. The grey shading represents the total concentration field c_t, with the line showing the contour $c_t = 0.1$. While B1 passes over the bump, B2 mostly flows around the bump.

that the lower sections of the current, i.e. the sections above the bottom boundary layer, are able to flow over bumps of height $h_b \lesssim 0.9$.

In order to validate the above scaling law, we conducted a series of simulations for compositional gravity currents interacting with bumps of different heights h_b, cf. figure 11. For $h_b = 1.25$ the bump fully bisects the current front, whereas for $h_b = 0.5$ part of the current still manages to flow over the top of the bump. This is confirmed by figure 12, which compares the current height computed in the y, z-plane at $x = 5.5$ (corresponding to the bump's peak) for several bump heights. For increasing bump heights we note that, while the current thickness at the peak of the bump decreases, it increases away from the bump.

To further investigate the dynamics of different vertical current sections during the interaction with the obstacle, fluid path lines for passive markers are shown in figure 13. These markers are initially located at $y = 0.1, 0.3, 0.5$ and 0.7 upstream of the bump at $x = 4.35$ in the symmetry plane at $z = 0.5L_z$. They are released at $t = 7$, and their path lines are integrated until $t = 20$.

The observed particle path lines are seen to be consistent with the above scaling law. For bump heights $h_b \lesssim 0.9$, even particles originating in the near-wall region are seen to be lifted over the top of the bump. On the other hand, for $h_b = 1.0$ the

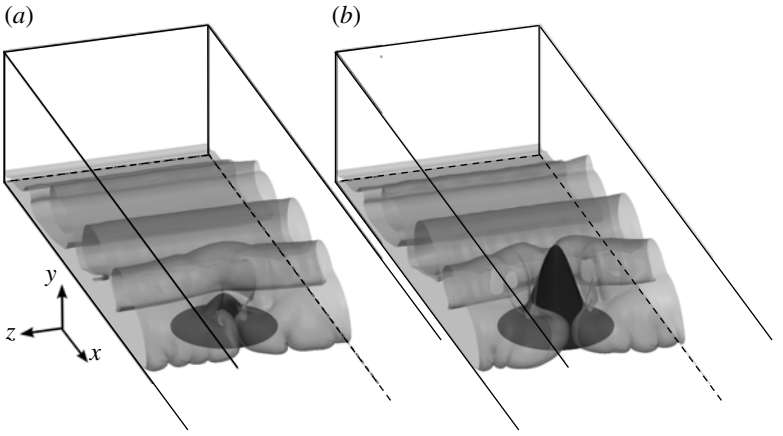

FIGURE 11. Isosurface of the concentration field $c = 0.1$ shown for two different bump heights at $t = 10$: (*a*) $h_b = 0.5$; (*b*) $h_b = 1.25$. The bottom section of the current is not able to fully cross-over the bump peak for $h_b \gtrsim 0.9$.

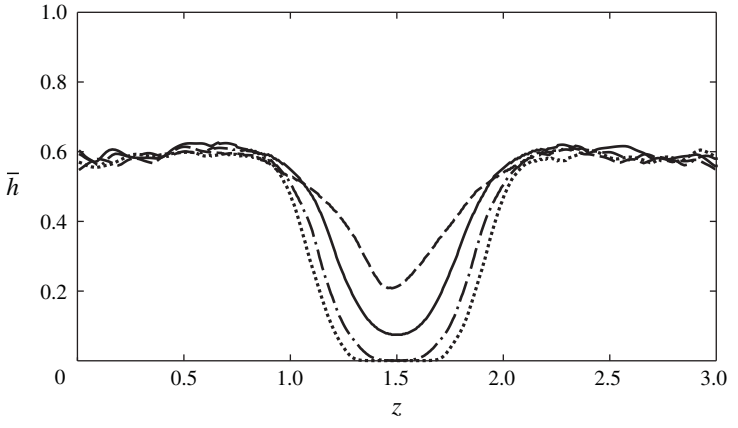

FIGURE 12. Comparison of current heights in the plane of the bump peak, for gravity currents interacting with bumps of different heights. Dashed line, solid line, dash-dots and dots correspond to bump heights of $h_b = 0.5, 0.75, 1.0$ and 1.25, respectively. The current height is averaged over the time interval from $t = 8$ to $t = 12$.

marker released at $y = 0.1$ travels around the bump, rather than over it. We furthermore observe that fluid marker particles released near the top of the current experience strong recirculating motion, indicative of the concentrated vortical structures forming in the mixing layer between the current and the ambient.

In order to analyse how the above observations for compositional gravity currents are modified due to the presence of a settling velocity, figure 14 compares fluid path lines for turbidity currents B1 and B2, for the same initial marker positions as before. Unlike for the compositional gravity current case B2-GC, the lowest marker for turbidity current B2 does not advance over the peak of the bump. This is a consequence of the lower height h_c (see (5.2)) of turbidity current B2 as compared with gravity current B2-GC. In addition, the energy loss of the turbidity current due to the Stokes dissipation in the small-scale flow around the particles lowers the

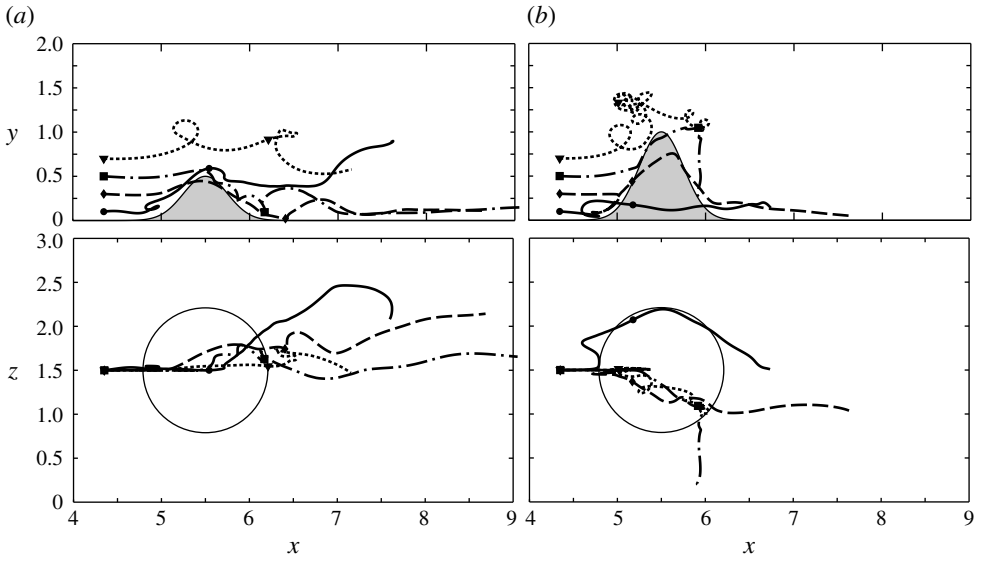

FIGURE 13. Fluid path lines for gravity currents interacting with Gaussian bumps of different heights. The fluid marker particles are released at $x = 4.35$ (in the symmetry plane $z = 1.5$) and time $t = 7$, and their locations are shown for times $t = 7$, 13 and 20. For $h_b = 1$, the fluid marker particles in the lower current sections are seen to flow around the bump rather than over it, consistent with the scaling law (see (5.2)): (*a*) $h_b = 0.5$; (*b*) $h_b = 1$.

current's capacity to travel over the obstacle. This will be analysed in further detail below, within the context of the energy budget discussion. We conclude that, for a given current height and velocity, the scaling law (5.2) represents an accurate criterion for compositional gravity currents, whereas it serves as an upper limit for turbidity currents.

When comparing the uppermost fluid path lines for gravity and turbidity currents interacting with bumps of various heights in figures 13 and 14, we recognize a stronger recirculating motion for the turbidity currents. This suggests that the turbidity currents give rise to more vigorous mixing of interstitial and ambient fluid, as compared with the gravity currents.

Figure 15 depicts selected in-plane streamlines for case B2 within the symmetry plane $z = 1.5$, in the laboratory reference frame. These indicate that the flow separates from the rear of the bump. However, due to the highly transient nature of the flow, this separation region is very short-lived, and periodic vortex shedding does not occur. The figure furthermore shows the spanwise vorticity component. Strong clockwise vortices exist in the bottom boundary layer. We draw particular attention to the boundary-layer vortex located near $x = 5$, which is just upstream of the bump. As this spanwise vortex is wrapped around the sides of the bump by the flow, it will be stretched in the streamwise direction, thus taking on the familiar structure of a horseshoe vortex (cf. Baker 1980), which is characterized by a downflow region in the wake of the bump. This behaviour is well-known from the flow of constant density boundary layers over obstacles (Baker 1978; Doligalski, Smith & Walker 1994).

At the same time, the mixing layer separating the current from the ambient counterflow above gives rise to counterclockwise Kelvin–Helmholtz (KH) vortices in the spanwise direction. We expect the interaction of these spanwise vortices with the

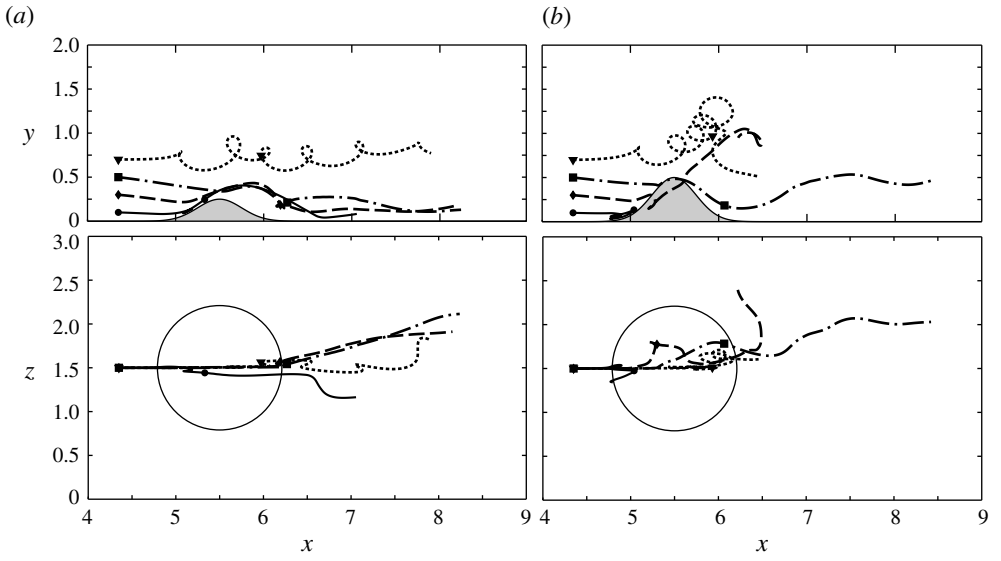

FIGURE 14. Fluid path lines shown for turbidity currents (*a*) B1 and (*b*) B2. Four seed markers released at $t = 7$ and $x = 4.35$ (in the symmetry plane $z = 1.5$) follow the fluid velocity until $t = 20$. The markers are also shown at time $t = 13$, indicating that the lowest marker is able to flow over the peak of the bump only for case B1, but not for case B2.

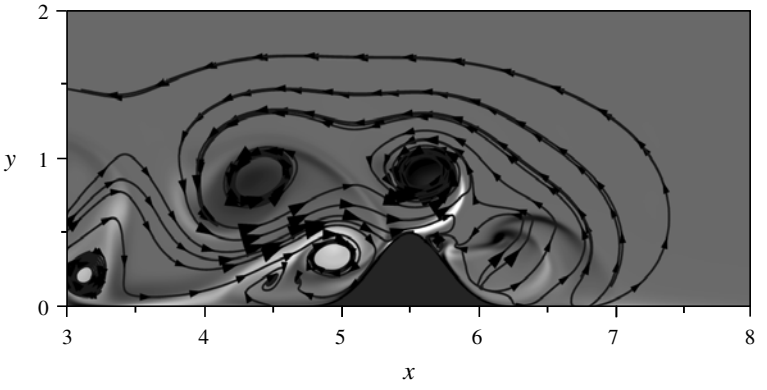

FIGURE 15. In-plane streamlines plotted in the symmetry plane $z = 1.5$, at $t = 11$ for case B2. Background shading represents the out-of-plane vorticity component w_z (black corresponding to $+15$, white to -15 and grey to zero). The separation and reattachment of the front are visible.

bump to result in the formation of streamwise vorticity as well. If the section of the KH vortex above the bump slows down compared with neighbouring sections, the resulting streamwise vorticity should be opposite in sign to that of the traditional horseshoe vortex, i.e. it should lead to an upflow region in the centre of the bump's wake. Conversely, if the KH vortex is accelerated above the bump, it should result in the formation of streamwise vorticity of the same sign as that of the horseshoe vortex.

This picture is confirmed by figure 16, which shows the streamwise vorticity along with the v- and w-velocity components for case B2 within two different $x = const.$

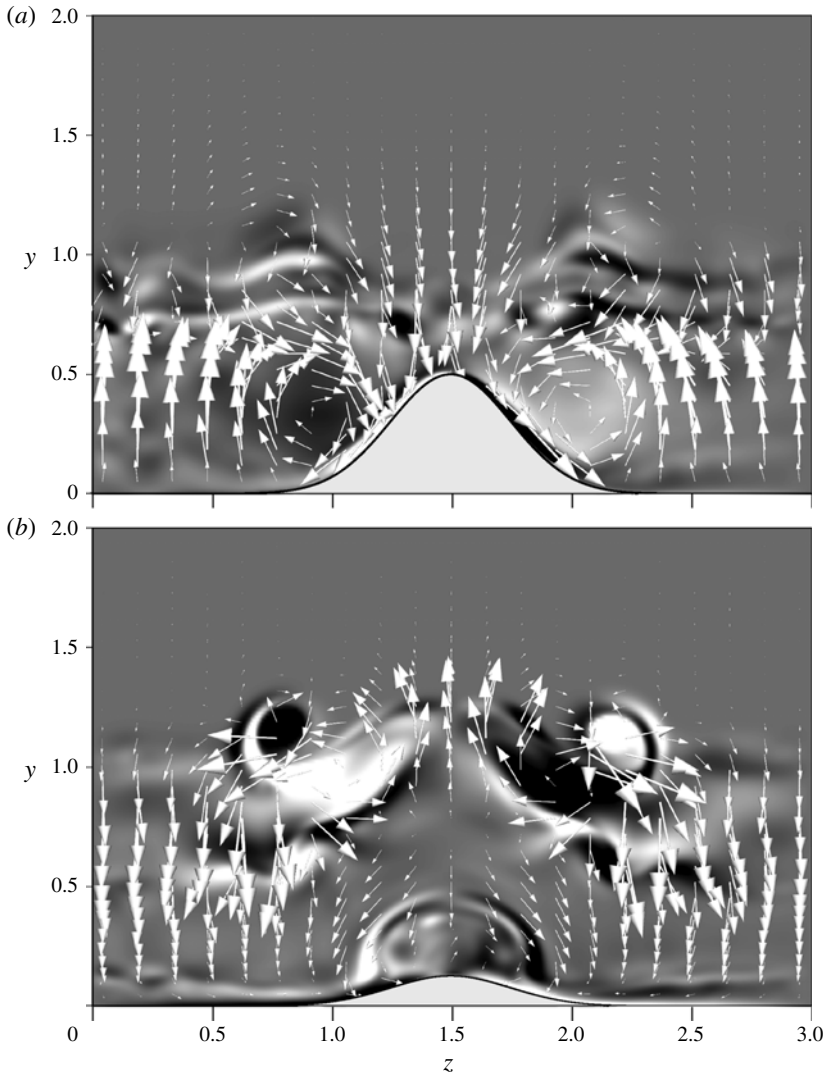

FIGURE 16. Streamwise vortical structure of current B2, illustrated by in-plane velocity vectors and the out-of-plane streamwise vorticity component ω_x (black, $+8$; white, -8; and grey, 0), at $t = 13$. In (*a*) the flow in the plane $x = 5.5$ is dominated by a traditional horseshoe vortex with a downwash at the centre, whereas in (*b*) the streamwise vortex pair of the opposite sign dominates the plane $x = 5.9$. This vortex pair is likely created by the deformation of mixing layer vorticity.

planes. At $x = 5.5$ we observe two strong coherent vortical structures adjacent to the sides of the bump. Their sign, with a downwash region at the centre, is consistent with that of a classical horseshoe vortex formed from the boundary-layer vorticity (Doligalski *et al.* 1994). At $x = 5.9$, on the other hand, we find that a counter-rotating streamwise vortex pair of the opposite sign dominates the near-wall region, i.e. with an upwash region at the wake centre. This streamwise vortex pair likely originated from the mixing layer at the top of the turbidity current.

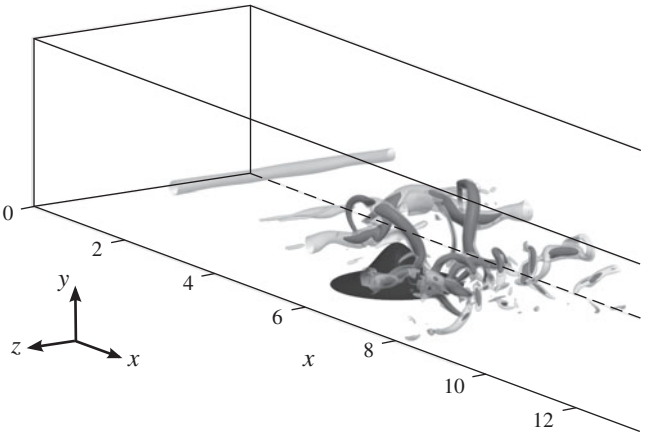

FIGURE 17. Vortical structures of turbidity current B2 visualized by isosurfaces of scalar Q (see (5.3)) at $t = 13$. Isosurfaces are shown for positive values of 10 (light grey) and 22 (dark grey). A strong streamwise vortex pair is seen to extend from the mixing layer all of the way down to the near-wall region in the wake of the bump.

We must keep in mind, however, that in addition to the convection, diffusion and stretching of vorticity we also have baroclinic vorticity production, as a result of the density difference between the current and the ambient. This mechanism most likely is responsible for the formation of the smaller, concentrated streamwise vortices visible at the top of the interface at $x = 5.9$.

To illustrate the three-dimensional nature of the vortical structures, we employ the familiar Q-criterion (Hunt, Wray & Moin 1988). The scalar quantity Q is defined based on the second invariant of the velocity gradient tensor $\boldsymbol{\nabla u}$ as

$$Q = \frac{1}{2}(\Omega_{mn}\Omega_{mn} - S_{mn}S_{mn}). \tag{5.3}$$

Here, Ω_{mn} and S_{mn} are the antisymmetric and symmetric components of $\boldsymbol{\nabla u}$

$$\Omega_{mn} = \frac{1}{2}\left(\frac{\partial u_m}{\partial x_n} - \frac{\partial u_n}{\partial x_m}\right), \tag{5.4}$$

$$S_{mn} = \frac{1}{2}\left(\frac{\partial u_m}{\partial x_n} + \frac{\partial u_n}{\partial x_m}\right), \tag{5.5}$$

respectively. Isosurfaces of a positive Q imply that the flow is locally dominated by fluid rotation, so that they allow us to visually identify vortex tubes. Figure 17 shows the structure of the vorticity field for case B2 at $t = 13$. We recognize a prominent pair of streamwise vortices that extend all of the way from the mixing layer at the top of the current, to the near-wall region in the wake of the bump. This is consistent with the streamwise vorticity shown in figure 16.

To gain insight into the influence of the Reynolds number, figure 4(*b*) compares the time-dependent front location for case B2-GC for the two different Reynolds number values of 2000 and 5000. While both currents initially travel with nearly identical speeds, the higher-Reynolds-number current is seen to be slightly faster after $t \approx 4$, due to lower dissipative losses. Consistent with the observations of other authors, we

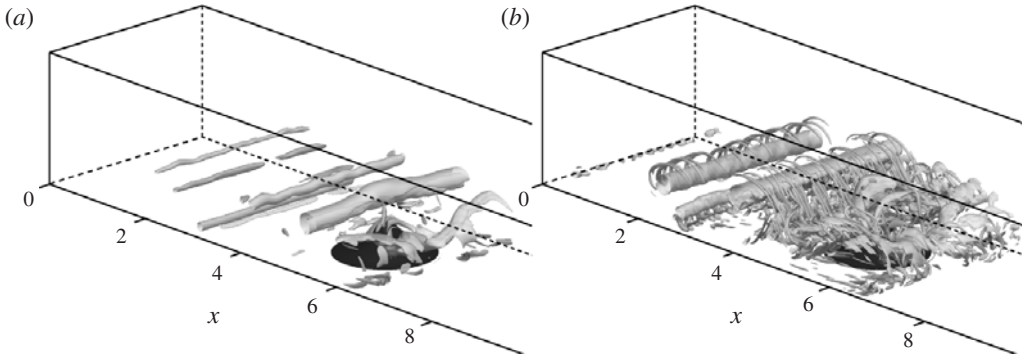

FIGURE 18. Vortical structures for case B2-GC at $t = 10$, for (*a*) $Re = 2000$ and (*b*) $Re = 5000$. While the large-scale structures are similar for both flows, the higher-Reynolds-number flow generates more fine-scale structure, as expected.

find that for Reynolds numbers above $O(1000)$ the front velocity depends only weakly on Re (Simpson & Britter 1979; Cantero *et al.* 2007). Figure 18 demonstrates the turbulent structures in the current shown by the Q-criterion (see (5.3)) during the interaction of the current with the bump. The large-scale structures are similar for both cases, while the higher-Reynolds-number case is seen to generate more fine-scale structure.

Figure 19 compares the temporal evolution of the lobe-and-cleft structures for the two Reynolds numbers. In both cases we observe the development of spanwise periodic lobe-and-cleft instabilities upstream of the bump, with a somewhat shorter wavelength for the higher Reynolds number. The strongly nonlinear evolution triggered by the interaction with the bump, which involves the merging, splitting and meandering of lobes, subsequently results in significantly wider lobes downstream of the bump for the lower Re value. Härtel *et al.* (2000*a*) employed a linear stability analysis to predict the growth rate and wave length of the lobes as a function of $Sc \times Re$. For the present Reynolds numbers (and $Sc = 1$), we find the most unstable wave numbers to be, respectively, $\beta_{Re=2000} \approx 30$ and $\beta_{Re=5000} \approx 53$ (see figure 6 of Härtel *et al.* 2000*a*). These values correspond to wavelengths of $\lambda = 2\pi/\beta$ equal to $\lambda_{Re=2000} = 0.21$ and $\lambda_{Re=5000} = 0.12$. The present simulation results upstream of the bump are fully consistent with these values, as they show dominant wave numbers of $\lambda^s_{Re=2000} = 0.214$ and $\lambda^s_{Re=5000} = 0.125$, respectively.

5.1. *Lateral deflection*

To quantify the lateral deflection of the current as it interacts with the bump, we employ the vertically integrated, streamwise concentration flux $\overline{uc}$ as a function of the spanwise location

$$\overline{uc}(z) = \int_{y=y_\Gamma}^{L_y} uc_t \,\mathrm{d}y. \tag{5.6}$$

Figure 20 compares the temporal evolution of $\overline{uc}(z)$ for all three cases, in the peak plane $x = 5.5$. We recognize that both at $t = 8$, when the front is just passing over the bump, and at $t = 14$, when the front has travelled quite a distance further downstream, the flux over the obstacle is somewhat reduced for case B1, and strongly reduced for

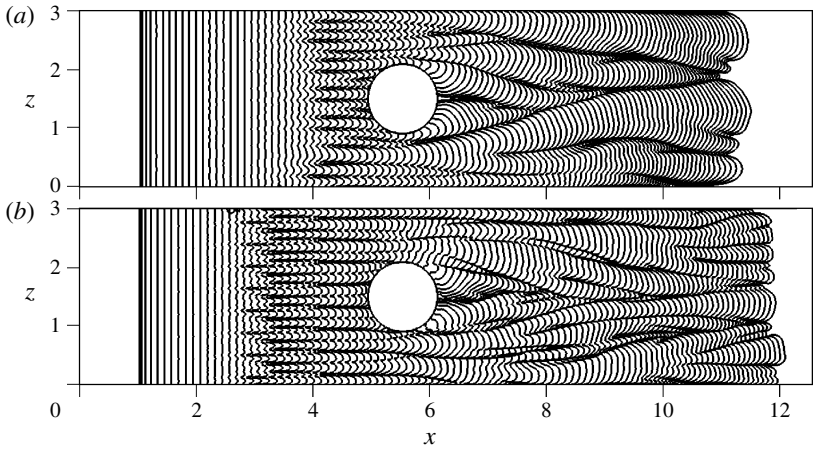

FIGURE 19. The formation, merging, splitting and meandering of lobe-and-cleft structures as shown by concentration contours of $c = 0.05$ at the bottom surface for case B2-GC at the two different Reynolds numbers of (*a*) $Re = 2000$ and (*b*) $Re = 5000$. The contour lines are indicated for time intervals of $\Delta t = 0.2$ until $t = 20$.

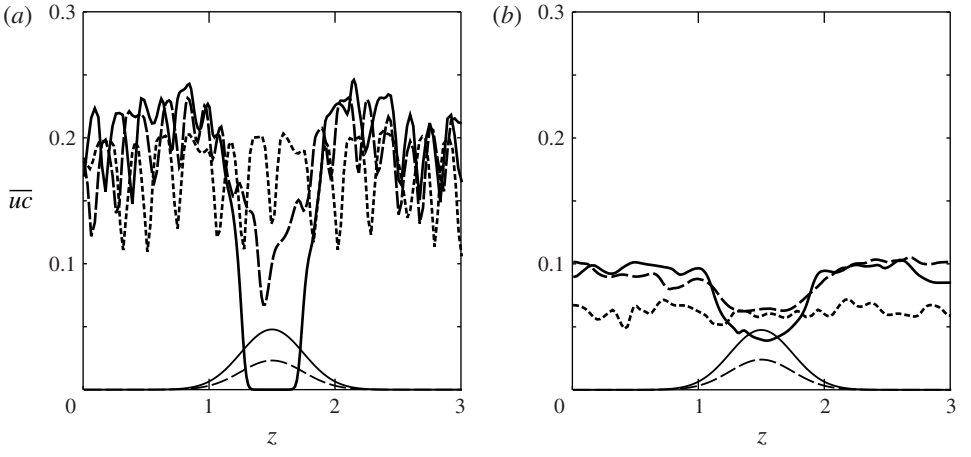

FIGURE 20. Streamwise concentration flux $\overline{uc}$ at $x = 5.5$, for all three currents at times (*a*) $t = 8$ and (*b*) $t = 14$. A comparison of cases FL (dots), B1 (dashed lines) and B2 (solid lines) shows that the lateral deflection of the current reduces the flux over the bump somewhat for B1, and strongly for B2, while enhancing the flux on the sides of the bumps.

case B2, as compared with the flat plate case FL. By contrast, the regions on each side of the bump see enhanced streamwise flux. We remark that the strong spanwise oscillations at $t = 8$ are due to the presence of the lobe-and-cleft instability, and the development of spanwise deformations of the mixing layer above the turbidity current.

In order to investigate the influence of the lateral domain boundaries, we repeated simulation B2-GC with twice the computational domain width, i.e. $L_z = 6$. Figure 21 compares the current height in the y, z-plane at the x location of the peak. The current heights are comparable near $z = 0$ and 3, indicating a minor influence of the lateral

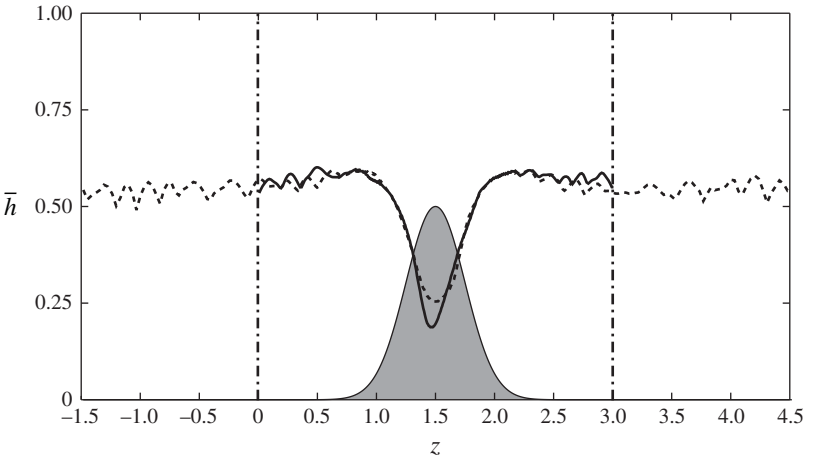

FIGURE 21. Current height in the y, z-plane $x = 5.5$ for case B2-GC and two different control volume widths $L_z = 3$ (solid line) and $L_z = 6$ (dashed line). The results are averaged in time from $t = 8$ to $t = 10$. The current height above the peak is somewhat lower for the narrower control volume, while the current height near $z = 0$ and 3 is similar for both control volumes, indicating a relatively small influence of the lateral boundaries.

boundaries for the flow in the narrower domain. Right above the peak of the bump, the narrower current shows a lower depth.

To summarize, consistent with earlier work on gravity currents propagating over flat boundaries, we find that the front velocity of currents interacting with three-dimensional bottom topography is only weakly affected by the value of the Reynolds number, as long as $Re \geqslant O(1000)$. The lobe-and-cleft structures, on the other hand, show a stronger influence of the Reynolds number. The current/bump interaction is seen to deform the bottom boundary layer vorticity into traditional horseshoe vortices, and the opposite-sign mixing layer vorticity into inverted horseshoe vortices. Additional streamwise vortical structures form as a result of baroclinic vorticity generation. Based on balance arguments for the kinetic and potential energy components, we are able to derive a scaling law for the maximum bump height that can be overcome by gravity currents. For turbidity currents, this estimate represents an upper limit.

6. Bottom shear stress and potential for erosion

In order to assess the potential of the current for triggering bedload transport and resuspension, the wall-shear stress distribution along the bottom boundary provides important information. Ultimately, the distances over which turbidity currents travel, and the stratigraphy they produce, depend strongly on this quantity. We record the wall-shear stress in terms of the friction velocity

$$u_\tau = \frac{\hat{u}_\tau}{\hat{u}_b} = \sqrt{\frac{1}{Re}\frac{\partial u_t}{\partial \eta_n}\bigg|_{y=y_\Gamma}}. \tag{6.1}$$

Here, u_t and η_n denote the velocity component tangential to the wall, and the wall-normal distance, respectively.

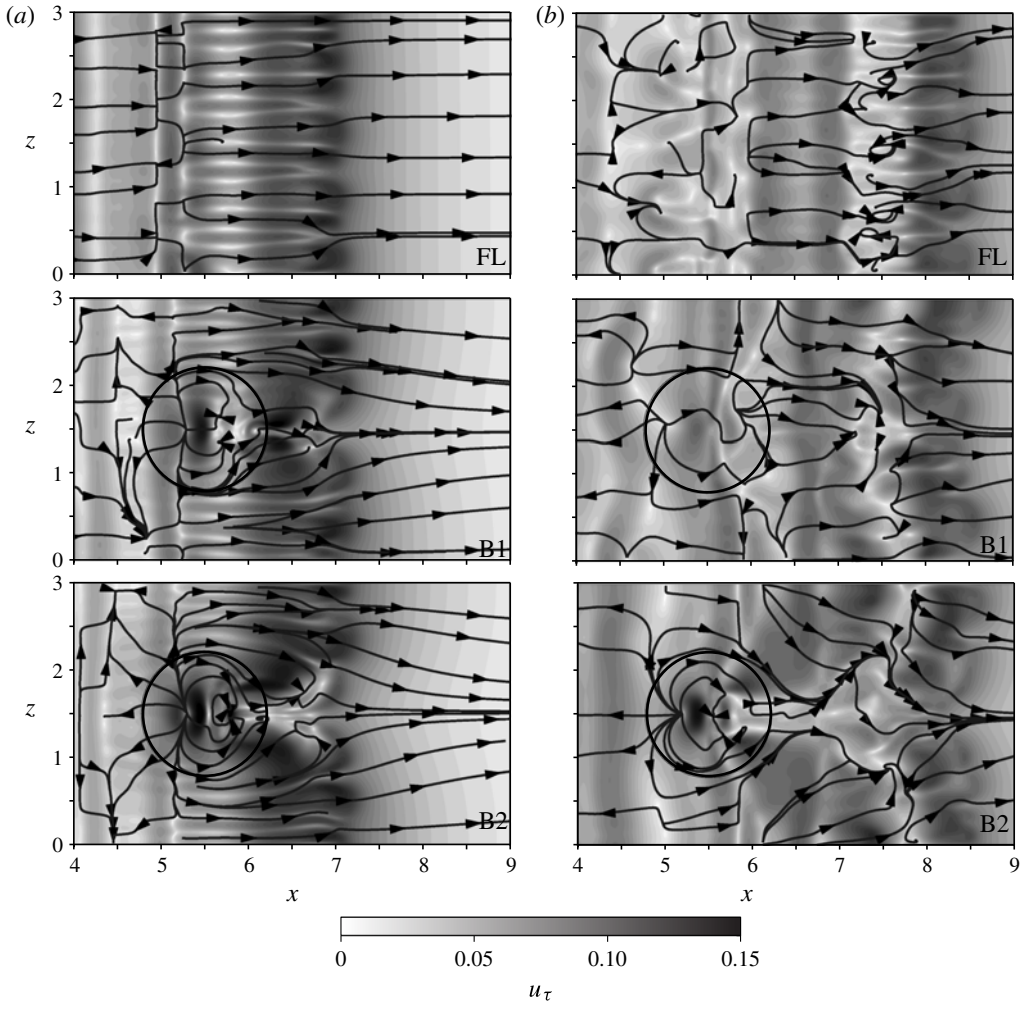

FIGURE 22. Magnitude of the friction velocity u_τ (grey shading) for cases FL, B1 and B2 at times (*a*) $t = 10.8$ and (*b*) $t = 14$. The lines represent the directional field of the instantaneous wall-shear stress. The vortical structures in the wake of the bump strongly modify the friction velocity field.

Figure 22 compares the instantaneous wall-shear stress for cases FL, B1 and B2 at two different times. We observe that for all flows the streamwise vortices associated with the lobe-and-cleft instabilities give rise to longitudinal streaks in the shear stress pattern. Even for currents B1 and B2, away from the bump these structures are maintained for some time after the current front passes the bump, cf. figure 22(*a*). For B1 and B2, a region of strong wall-shear stress exists just upstream of the peak at $t = 10.8$. Along the centreline of the bump's wake the shear stress is reduced, indicating an area of flow separation or reattachment. To the sides of this separation region, the wall-shear stress is enhanced. A comparison of the wall-shear stress patterns for cases B1 and B2 demonstrates the tendency of the flow to go around the taller bump, whereas it tends to move over the smaller bump, cf. figure 22(*b*).

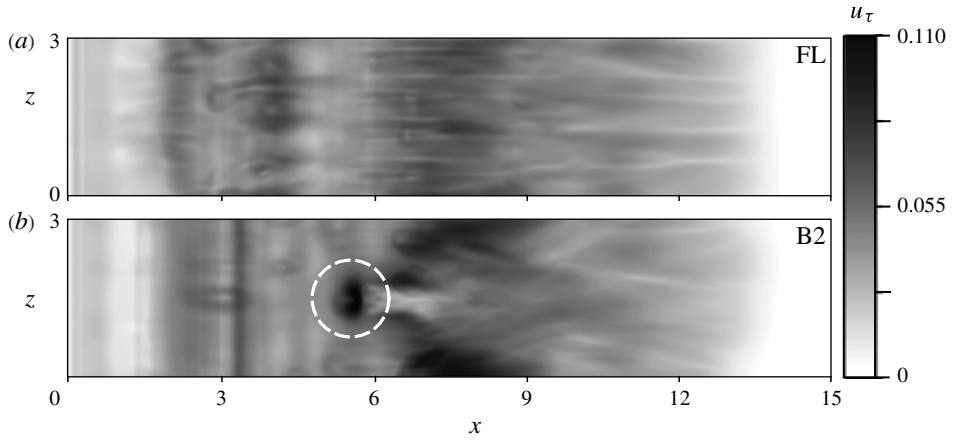

FIGURE 23. Magnitude of the friction velocity u_τ averaged from $t = 10$ to $t = 30$. Regions with high average wall-shear stress exist near the top of the bumps for B1 and B2, and to the sides of the wake centreline for B2.

Figure 23 compares the u_τ values averaged from $t = 10$ to $t = 30$. Case FL is characterized by long, fairly straight and evenly spaced streaks behind the front, due to lobe-and-cleft instabilities. Occasionally, these streaks are seen to merge. For cases B1 and B2, streaks also exist downstream of the bump, but they are not as straight and as evenly spaced as for FL. The vicinity of the bump's peak exhibits strong time-averaged shear, indicating that it might get preferentially eroded if erosion were included in the simulation. For case B2, further regions of high wall-shear stress appear near the spanwise boundaries downstream of the bump, which suggests that the existence of these boundaries may influence the flow to some extent for case B2.

A comparison of the wall-shear stress levels for case B2-GC with control volume widths of $L_z = 3$ and 6 shows slightly elevated shear stress levels near the side walls for the narrow control volume. However, the overall main shear stress pattern in the wake is seen to be largely unaffected by the side walls. For $Re = 5000$ the wall-shear stress field is more uniform, and reduced in magnitude, as compared with $Re = 2000$.

6.1. *Potential for erosion*

Several approaches are available in the literature to estimate the critical shear stress level beyond which incipient particle motion can occur. Towards this end, we employ the particle Reynolds number Re_* and the Shields parameter Υ

$$Re_* = \frac{\hat{u}_\tau \hat{d}_p}{\hat{\nu}}, \tag{6.2}$$

$$\Upsilon = \frac{\hat{\rho}\hat{u}_\tau^2}{(\hat{\rho}_p - \hat{\rho})\hat{g}\hat{d}_p}. \tag{6.3}$$

A critical value of Υ_{cr} as a function of Re_* is suggested by Yalin & Karahan (1979). In order to apply their criterion, we need to employ dimensional quantities. To relate the above simulations to a typical laboratory-scale experiment, we choose a channel height of $\hat{H} = 0.2$ m. We further assume the ambient fluid to be water with room

temperature properties (i.e. $\hat{\rho}_0 = 1000$ kg m^{-3}, $\hat{\nu} = 10^{-6}$ m^2 s^{-1}). We consider particles of spherical shape with a material density of $\hat{\rho}_p = 2500$ kg m^{-3} (this density is an appropriate choice for turbidity currents forming on the continental slopes and/or many submarine fans; cf. Normark, Posamentier & Mutti 1993). Using our definition of the Reynolds number in (2.3), the buoyancy velocity is computed as $\hat{u}_b = 0.02$ m s^{-1}. Furthermore, we assume the particle settling velocity to be equal to the Stokes value (see (2.5)) for spherical particles. Thus, we obtain coarse and fine particle diameters of $\hat{d}_p^c = 27$ μm and $\hat{d}_p^f = 12$ μm.

Using the maximum shear stress value of $u_\tau = 0.11$ from figure 23, we obtain values of $Re_* = 0.0594$ and 0.0264, and $\Upsilon = 0.0122$ and 0.0274, for coarse and fine particles, respectively. According to Yalin & Karahan (1979), for the above values of Re_*, the corresponding critical thresholds are $\Upsilon_{cr} = 0.2$ and 0.25, respectively. These values are well above those obtained above, which suggests that incipient particle motion is unlikely to occur.

In general, our choice of dimensionless parameters corresponds to laboratory scales. In natural settings, however, typical Reynolds numbers are significantly higher, which will alter the above critical values.

7. Energy budgets

A gravity current is characterized by the conversion of potential into kinetic energy. Eventually, the current will come to rest as this kinetic energy is dissipated by viscosity. In particle-laden currents, it is useful to distinguish between the viscous dissipation that occurs at the macroscopic scales, and the dissipative losses in the microscopic Stokes flow around each particle. While the former is fully resolved in the current simulations, the latter is accounted for only indirectly, through the settling motion of the particles.

In this section, we examine how the temporal evolution of the different energy components is affected by the current's interaction with the bottom topography. Towards this goal, we employ the kinetic and potential energy equations, in following the approach applied by Necker *et al.* (2005) for currents propagating over a flat bottom wall. For the detailed derivation of the various terms in the energy equation, we refer the reader to this earlier work. We obtain for the rate of change of the total mechanical energy of the flow

$$\frac{\mathrm{d}}{\mathrm{d}t}(E_k + E_p) = -\int_\Omega \frac{2}{Re} S_{mn} S_{mn}\,\mathrm{d}V - \sum_{i=1}^{2}\left(\int_\Omega u_s^i c_i\,\mathrm{d}V\right) - \sum_{i=1}^{2}\left(-\int_A y_\Gamma u_s^i c_w^i \boldsymbol{e}^g \cdot \boldsymbol{n}\,\mathrm{d}A\right), \tag{7.1}$$

where E_k and E_p denote the kinetic and potential energy components, respectively. We can interpret the last term on the right-hand side of (7.1) as the loss of potential energy due to settling of particles at locations along the bottom boundary with non-zero height (y_Γ), cf. figure 2.

In (7.1), the loss of mechanical energy can be linked to three mechanisms, namely the loss due to viscous dissipation at macroscopic scales ϵ_d, the loss due to viscous effects in the microscopic Stokes flow around each particle ϵ_s, and the deposition of particles along the bottom boundary ϵ_l

$$\epsilon_d = \int_\Omega \frac{2}{Re} S_{mn} S_{mn}\,\mathrm{d}V \tag{7.2}$$

$$\epsilon_s = \sum_{i=1}^{2} \left(\int_{\Omega} u_s^i c_i \, \mathrm{d}V \right) \tag{7.3}$$

$$\epsilon_l = \sum_{i=1}^{2} \left(- \int_{A} y_\Gamma u_s^i c_w^i \boldsymbol{e}^g \cdot \boldsymbol{n} \, \mathrm{d}A \right). \tag{7.4}$$

Integrating (7.1) with respect to time yields

$$E_k + E_p + E_d + E_s + E_l = \text{const.} = E_{p0} + E_{k0} = E_t, \tag{7.5}$$

with

$$E_d = \int_0^t \epsilon_d(\tau) \, \mathrm{d}\tau, \tag{7.6}$$

$$E_s = \int_0^t \epsilon_s(\tau) \, \mathrm{d}\tau, \tag{7.7}$$

$$E_l = \int_0^t \epsilon_l(\tau) \, \mathrm{d}\tau, \tag{7.8}$$

and E_{p0} and E_{k0} representing the initial potential and kinetic energy available in the domain. We remark that in the present investigation the flow starts from rest, so that $E_{k0} = 0$. A discussion of the effects of initial turbulent kinetic energy on the subsequent flow is provided by Necker *et al.* (2002) and Necker *et al.* (2005). We remark that in the present study, we ignore the influence of particle diffusion on the potential energy. For a detailed discussion of such effects, see Winters *et al.* (1995) and Espath *et al.* (2014).

Figure 24 shows the time history of all energy components for case B1. During the early stages after the lock release, we observe a rapid conversion of potential into kinetic energy, which reaches its peak at $t \approx 5$. Subsequently, the potential and kinetic energy components both decline as a result of viscous dissipation. While the microscopic Stokes dissipation initially slightly outweighs the viscous dissipation at the large scales, this trend reverses after $t \approx 15$. By the final time of the simulation, $\sim$56 % of the initial potential energy has been dissipated at the macroscopic scales, and $\sim$41 % has been lost in the microscopic flow around the particles. The loss due to the settling of particles on the bump (E_l) is of $O(1\,\%)$, since the bump occupies only a small fraction of the entire bottom boundary, and comparatively few particles are deposited in this region.

Figure 25(*a*) compares the kinetic and potential energy for flows FL, B1 and B2. We observe that cases FL and B1 show very similar behaviour for all times. After the current front has passed over the bump ($t \geqslant 10$), the kinetic energy decreases more rapidly for B2 as compared with FL and B1. Partly this is due to the fact that some of the current fluid gains potential energy. However, figure 25(*b*) indicates that the energy E_d dissipated at the macroscopic scales is also larger for B2 than it is for FL and B1, due to the pronounced streamwise vorticity generation for $t \geqslant 10$ resulting from the interaction of the mixing layer with the bump (see figure 17). On the other hand, the viscous energy losses in the microscopic flow around the particles are nearly identical for FL, B1 and B2.

Figure 26 displays the temporal evolution of the energy components for cases B2 and B2-GC. Until $t \approx 4$, the potential and kinetic energy curves are very similar.

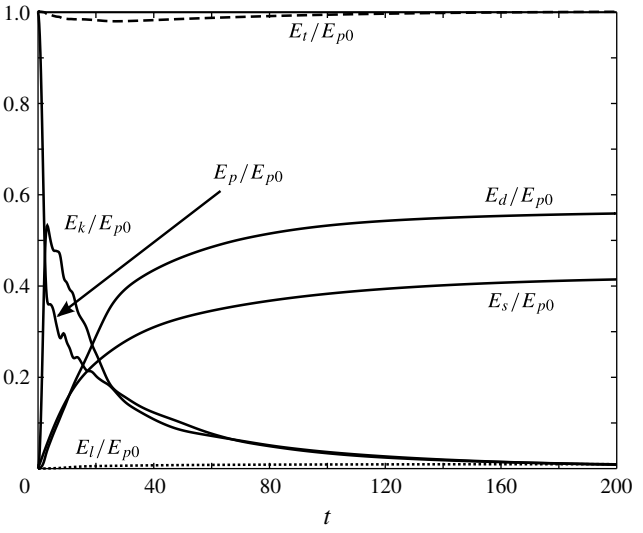

FIGURE 24. Time history of potential energy E_p, kinetic energy E_k, dissipation components E_d and E_s, and the energy loss E_l due to particle settling on the bump. All energies are normalized by the initial potential energy E_{p0}. Total energy E_t verifies total energy conservation. Results are from simulation B1.

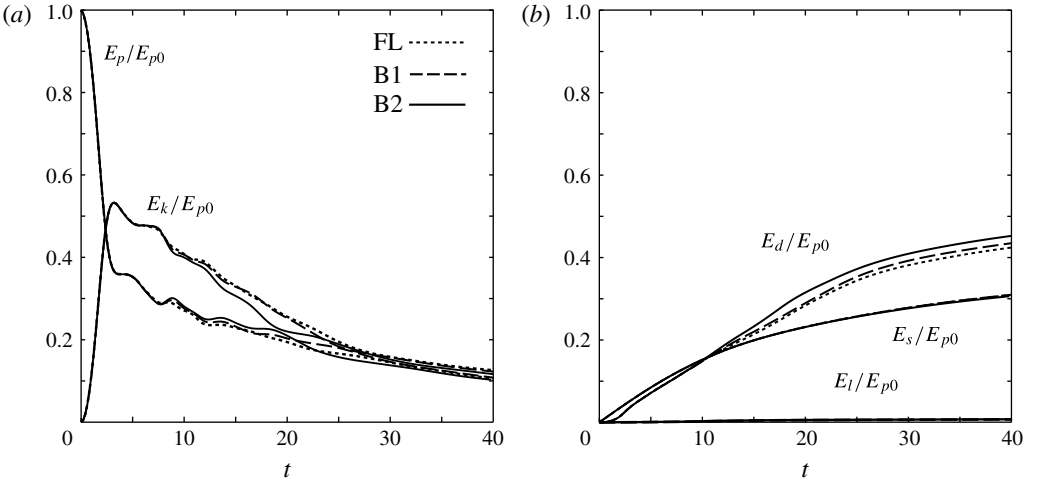

FIGURE 25. Temporal evolution of the energy budgets normalized by the initial potential energy for simulations Fl, B1, and B2. (*a*) Kinetic E_k and potential energy E_p. (*b*) Energy loss components including viscous dissipation E_d, Stokes dissipation E_s and depositional loss E_l.

Thereafter, the loss of particles and forward momentum reduces the kinetic and potential energy components for turbidity current B2. Figure 26(*b*) compares the viscous (E_d) and Stokes (E_s) dissipation components. We note that E_s is present only in the turbidity current B2 (see (7.3)). At $t \approx 10$, the viscous dissipation component E_d produced in case B2-GC surpasses its B2 counterpart, and it subsequently maintains

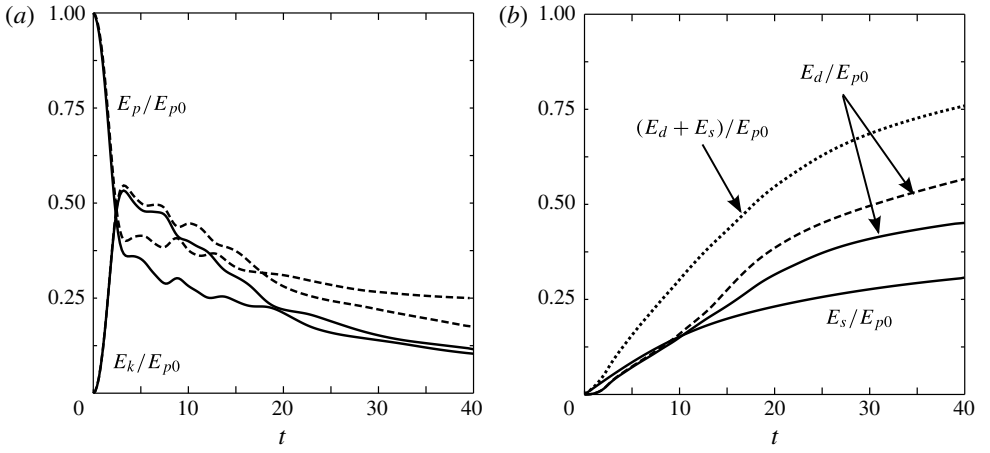

FIGURE 26. Time history of the various energy budget components shown for case B2 (solid lines and dots) and B2-GC (dashed lines). (*a*) Kinetic and potential energy components. (*b*) Viscous and Stokes dissipation.

higher values for the remainder of the simulation. This is a consequence of the higher kinetic energy levels of the gravity current which lead to stronger dissipative energy loss.

The total energy loss in case B2 (dots in figure 26*b*) including the Stokes dissipation E_s (which is absent in case B2-GC) exceeds that of case B2-GC from the start. By time 40, 75 % of the total initial potential energy has been lost to dissipation in case B2. Gravity current B2-GC, on the other hand, retains approximately 45 % of the initial potential energy by $t = 40$, which allows it to travel farther downstream.

In summary, the influence of the bottom topography is seen to be non-monotonic. The tallest bump simulation exhibits the highest levels of streamwise vorticity during the interaction stages, whereas during the late stages these levels drop below those for the flat bottom simulation. As expected, currents interacting with taller bumps dissipate more energy, as compared with currents propagating over lower bumps or flat bottoms.

8. Discussion and conclusions

8.1. *Applicability to field-scale currents*

As it is both difficult and costly to conduct field-scale measurements of turbidity currents in natural settings (Xu, Noble & Rosenfeld 2004), the question arises as to how much insight can be gained from laboratory or simulation data into field-scale flows. The two main dimensionless parameters characterizing turbidity currents are the Reynolds and Froude numbers. For sufficiently large values of $Re > O(1000)$, certain properties of turbidity currents, such as their non-dimensional front velocity and frontal shape, are known to depend only weakly on Re. The shear stress and turbulence properties of the bottom boundary layer, on the other hand, are strong functions of Re, which consequently also applies to their ability to erode sediment, and hence to their runout length.

The Froude number $Fr = U/\sqrt{g'h}$ (with U, h and g' representing the velocity and height of the current and the reduced gravity, respectively) can have a significant influence on the general properties of gravity currents, as discussed by Sequeiros *et al.*

(2010) in the context of supercritical versus subcritical currents, cf. also Pirmez & Imran (2003). Supercritical currents tend to have the velocity maximum close to the sediment bed, while subcritical ones exhibit milder velocity and density gradients in this region.

In summary, while Froude number similarity appears to be essential for upscaling laboratory flows, such small flows cannot be expected to duplicate the erosional behaviour and runout length of field-scale currents due to limitations in the Reynolds number.

8.2. *Non-monotonic behaviour*

Early on in our analysis, we had observed that the influence of the bottom topography on the front velocity of turbidity currents is significantly weaker than the influence of the particle settling velocity. However, we had noticed an interesting non-monotonic behaviour, in that the current interacting with a bump of intermediate height advanced more rapidly than its counterparts propagating over a flat bottom or interacting with a tall bump. Based on the above information regarding the spatiotemporal evolution of the concentration and dissipation fields, we can now obtain insight into the mechanisms that lead to this non-monotonic influence of the bump height on the late-stage front velocity. Figure 27(*a*) compares the front velocities

$$U_f = \frac{\mathrm{d}x_f}{\mathrm{d}t} \tag{8.1}$$

of currents FL, B1, B2 and B2-GC. Around $t \approx 8$, as the front begins to interact with the bump, we observe an increase of the front velocity with the bump height. This is a direct result of the lateral deflection of the currents by the bump, which leads to an effective increase in the current height

$$\bar{h}(x, z) = \int_{y_\Gamma}^{L_y} c_t(x, y, z)\, \mathrm{d}y \tag{8.2}$$

in the regions between the bump and the lateral domain boundaries. This is clearly recognizable in figure 27(*b*), which shows that successively taller bumps reduce the effective current height above the bump, but increase it in the regions to the side of the bump. Thus, the streamwise hydrostatic pressure gradient driving the current increases in these regions, which in turn accelerates the current front. This increase in the current height is also consistent with the increase in the potential energy of B1 and B2 seen in figure 25(*a*) around this time. We conclude that the presence of the bump effectively reduces the width of the flow domain available to the current, so that its height increases.

A short time later, however, all currents begin to slow down. We note that B2 decelerates more rapidly than FL and B1, and by $t \approx 12$, B2 exhibits the lowest front velocity of all currents. This is consistent with figure 25(*b*), which shows that beyond $t \gtrsim 12$, B2 displays a higher rate of dissipation than FL and B1. This increased dissipation is a consequence of the strongly three-dimensional nature of the flow, resulting from the current's interaction with the tall bump as described above. It reduces the kinetic energy of current B2 as compared with currents FL and B1, cf. figure 25(*a*), which undergo less-vigorous three-dimensional evolutions, and hence have lower dissipation rates. As a result, for late times B2 has the lowest front velocity of all currents, cf. figure 27(*a*).

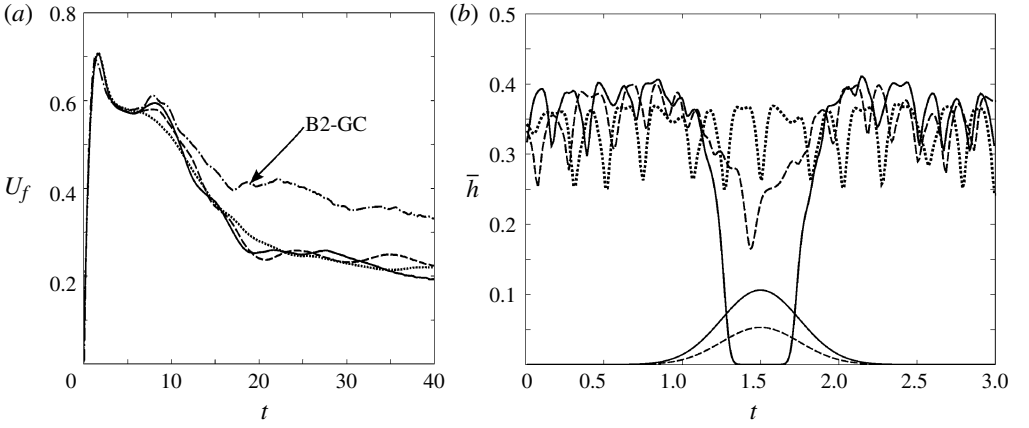

FIGURE 27. (*a*) Time history of the front velocities for currents FL (dots), B1 (dashed line), B2 (solid line) and B2-GC (dash-dotted line). As the current arrives at the bump and is deflected laterally, its height increases in the regions to the side of the bump, which in turn results in an increase of the front velocity. (*b*) Current height $\bar{h}$ in the plane $x = 5.5$ shown at $t = 8$. Dots, dashed line and solid lines represent cases FL, B1 and B2, respectively. The current height is reduced above the bump, but increases in the regions to the side of the bump. Consequently, the streamwise hydrostatic pressure gradient driving the flow increases in these regions, and the current front accelerates.

In summary, the following picture emerges: the lateral deflection of the current by the bump leads to an effective increase in the current height, and hence its front velocity, with the bump height. At the same time, taller bumps result in a more vigorous three-dimensional evolution of the currents, accompanied by increased rates of dissipation, which tend to slow down the currents. For relatively small bumps, the former mechanism dominates, so that on average the current front propagates faster than its flat bottom counterpart. For currents interacting with larger bumps, on the other hand, the increased dissipation becomes dominant, so that they exhibit a reduced front velocity as compared with currents over flat surfaces.

The above analysis demonstrates that the interaction of turbidity currents with three-dimensional seafloor topography gives rise to a variety of mechanisms that frequently tend to favour opposing outcomes with regard to their mixing dynamics and rate of propagation. Hence, the spatiotemporal evolution of turbidity currents can react quite sensitively to specific topographical features. It will be interesting to explore how the current/seafloor interaction is affected by the presence of erosion, resuspension and bedload transport.

Acknowledgements

We acknowledge helpful discussions with Professor Ben Kneller on the physics of turbidity currents propagating over complex topography. We also thank the three anonymous referees for their insightful suggestions and comments which helped improve this work. MN was partially funded via research support to Professor Kneller's group from BG Group, BP, ConocoPhillips, DONG, GDF Suez, Hess, Petrobras, RWE Dea, Total and Statoil. EM acknowledges financial assistance through the NSF (grant numbers CBET-0854338, CBET-1067847 and OCE-1061300). The simulations were carried out at the Janus, Epic and Beach supercomputing facilities.

Janus is supported by the National Science Foundation (award number CNS-0821794) and the University of Colorado at Boulder and is a joint effort of the University of Colorado Boulder, the University of Colorado Denver and the National Centre for Atmospheric Research. The Epic@iVec supercomputing facility is part of the Pawsey Centre project of the iVec Institute, Australia. Access to the Beach cluster was provided by the Community Surface Dynamics Modelling System (CSDMS) high-performance computing facility at the University of Colorado in Boulder.

REFERENCES

AL JA AIDI, O. S. 2000 The influence of topography and flow efficiency on the deposition of turbidites. PhD thesis, University of Leeds.

ARMI, L. 1986 The hydraulics of two flowing layers with different densities. *J. Fluid Mech.* **163** (1), 27–58.

BAKER, C. J. 1978 Vortex flow around the bases of obstacles. PhD thesis, University of Cambridge.

BAKER, C. J. 1979 The laminar horseshoe vortex. *J. Fluid Mech.* **95** (02), 347–367.

BAKER, C. J. 1980 The turbulent horseshoe vortex. *J. Wind Engng Ind. Aerodyn.* **6** (1), 9–23.

BELCHER, S. E. & HUNT, J. C. R. 1998 Turbulent flow over hills and waves. *Annu. Rev. Fluid Mech.* **30** (1), 507–538.

BENJAMIN, T. B. 1968 Gravity currents and related phenomena. *J. Fluid Mech.* **31** (2), 209–248.

BIRMAN, V. K., MARTIN, J. E. & MEIBURG, E. 2005 The non-Boussinesq lock-exchange problem. Part 2. High-resolution simulations. *J. Fluid Mech.* **537**, 125–144.

BLANCHETTE, F., STRAUSS, M., MEIBURG, E., KNELLER, B. & GLINSKY, M. E. 2005 High-resolution numerical simulations of resuspending gravity currents: conditions for self-sustainment. *J. Geophys. Res.* **110** (C12), C120–C122.

BONNECAZE, R. T., HUPPERT, H. E. & LISTER, J. R. 1993 Particle-driven gravity currents. *J. Fluid Mech.* **250**, 339–369.

BORDEN, Z. & MEIBURG, E. 2013 Circulation based models for Boussinesq gravity currents. *Phys. Fluids* **25** (10), 101301.

CANTERO, M. I., BALACHANDAR, S., CANTELLI, A., PIRMEZ, C. & PARKER, G. 2009 Turbidity current with a roof: direct numerical simulation of self-stratified turbulent channel flow driven by suspended sediment. *J. Geophys. Res.* **114** (C3), C03008.

CANTERO, M. I., LEE, J. R., BALACHANDAR, S. & GARCIA, M. H. 2007 On the front velocity of gravity currents. *J. Fluid Mech.* **586**, 1–39.

CASTRO, I. P. & SNYDER, W. H. 1993 Experiments on wave breaking in stratified flow over obstacles. *J. Fluid Mech.* **255**, 195–211.

CASTRO, I. P., SNYDER, W. H. & MARSH, G. L. 1983 Stratified flow over three-dimensional ridges. *J. Fluid Mech.* **135**, 261–282.

CHORIN, A. J. 1968 Numerical solution of the Navier–Stokes equations. *Maths Comput.* **22** (104), 745–762.

DADE, W. & HUPPERT, H. E. 1995 A box model for non-entraining, suspension-driven gravity surges on horizontal surfaces. *Sedimentology* **42** (3), 453–470.

DE ROOIJ, F. & DALZIEL, S. B. 2001 Time- and space-resolved measurements of the deposition under turbidity currents. *Special Publ. Int. Assoc. Sedimentol.* **31**, 207–215.

DIETRICH, W. E. 1982 Settling velocity of natural particles. *Water Resour. Res.* **18** (6), 1615–1626.

DOLIGALSKI, T. L., SMITH, C. R. & WALKER, J. D. A. 1994 Vortex interactions with walls. *Annu. Rev. Fluid Mech.* **26** (1), 573–616.

EIFF, O. S. & BONNETON, P. 2000 Lee-wave breaking over obstacles in stratified flow. *Phys. Fluids* **12**, 1073.

ELLISON, T. H. & TURNER, J. S. 1959 Turbulent entrainment in stratified flows. *J. Fluid Mech.* **6** (3), 423–448.

ESPATH, L. F. R., PINTO, L. C., LAIZET, S. & SILVESTRINI, J. H. 2014 Two-and three-dimensional direct numerical simulation of particle-laden gravity currents. *Comput. Geosci.* **63**, 9–16.

GARCIA, M. & PARKER, G. 1993 Experiments on the entrainment of sediment into suspension by a dense bottom current. *J. Geophys. Res.* **98** (3), 4793–4807.

GLADSTONE, C., PHILLIPS, J. C. & SPARKS, R. S. J. 1998 Experiments on bidisperse, constant-volume gravity currents: propagation and sediment deposition. *Sedimentology* **45** (5), 833–843.

GONZALEZ-JUEZ, E., MEIBURG, E. & CONSTANTINESCU, G. 2009 Gravity currents impinging on bottom-mounted square cylinders: flow fields and associated forces. *J. Fluid Mech.* **631**, 65.

GONZALEZ-JUEZ, E., MEIBURG, E., TOKYAY, T. & CONSTANTINESCU, G. 2010 Gravity current flow past a circular cylinder: forces, wall shear stresses and implications for scour. *J. Fluid Mech.* **649**, 69–102.

HALL, B., MEIBURG, E. & KNELLER, B. 2008 Channel formation by turbidity currents: Navier–Stokes-based linear stability analysis. *J. Fluid Mech.* **615**, 185–210.

HALLWORTH, M., HOGG, A. & HUPPERT, H. E. 1998 Effects of external flow on compositional and particle gravity currents. *J. Fluid Mech.* **359**, 109–142.

HARRIS, T. C., HOGG, A. J. & HUPPERT, H. E. 2002 Polydisperse particle-driven gravity currents. *J. Fluid Mech.* **472** (1), 333–371.

HÄRTEL, C., CARLSSON, F. & THUNBLOM, M. 2000*a* Analysis and direct numerical simulation of the flow at a gravity-current head. Part 2. The lobe-and-cleft instability. *J. Fluid Mech.* **418**, 213–229.

HÄRTEL, C., MEIBURG, E. & NECKER, F. 2000*b* Analysis and direct numerical simulation of the flow at a gravity-current head. Part 1. Flow topology and front speed for slip and no-slip boundaries. *J. Fluid Mech.* **418**, 189–212.

HARTEN, A. 1997 High resolution schemes for hyperbolic conservation laws. *J. Comput. Phys.* **135** (2), 260–278.

HARTEN, A., ENGQUIST, B., OSHER, S. & CHAKRAVARTHY, S. R. 1987 Uniformly high order accurate essentially non-oscillatory schemes, III. *J. Comput. Phys.* **71** (2), 231–303.

HUANG, H., IMRAN, J. & PIRMEZ, C. 2008 Numerical study of turbidity currents with sudden-release and sustained-inflow mechanisms. *J. Hydraul. Engng* **134** (9), 1199–1209.

HUNT, J. C. R. & SNYDER, W. H. 1980 Experiments on stably and neutrally stratified flow over a model three-dimensional hill. *J. Fluid Mech.* **96** (04), 671–704.

HUNT, J. C. R., WRAY, A. A. & MOIN, P. 1988 Eddies, stream, and convergence zones in turbulent flows. *Tech. Rep.* CTR-S88. Centre for Turbulence Research.

HUPPERT, H. E. 1986 The intrusion of fluid mechanics into geology. *J. Fluid Mech.* **173** (1), 557–594.

HUPPERT, H. E. & SIMPSON, J. E. 1980 The slumping of gravity currents. *J. Fluid Mech.* **99** (04), 785–799.

JANOCKO, M., CARTIGNY, M. B. J., NEMEC, W. & HANSEN, E. W. M. 2012 Turbidity current hydraulics and sediment deposition in erodible sinuous channels: laboratory experiments and numerical simulations. *Mar. Petrol. Geol.*

KANE, I. A., MCCAFFREY, W. D., PEAKALL, J. & KNELLER, B. C. 2010 Submarine channel levee shape and sediment waves from physical experiments. *Sedim. Geol.* **223** (1), 75–85.

KASSEM, A. & IMRAN, J. 2004 Three-dimensional modelling of density current. II. Flow in sinuous confined and uncontined channels. *J. Hydraul. Res.* **42** (6), 591–602.

KIM, J. & MOIN, P. 1985 Application of a fractional-step method to incompressible Navier–Stokes equations. *J. Comput. Phys.* **59** (2), 308–323.

KNELLER, B. & MCCAFFREY, W. D. 1999 Depositional effects of flow non-uniformity and stratification within turbidity currents approaching a bounding slope; deflection, reflection, and facies variation. *J. Sedim. Res.* **69** (5), 980–991.

KUBO, Y. 2004 Experimental and numerical study of topographic effects on deposition from two-dimensional, particle-driven density currents. *Sedim. Geol.* **164** (3–4), 311–326.

KUBO, Y. & NAKAJIMA, T. 2002 Laboratory experiments and numerical simulation of sediment-wave formation by turbidity currents. *Mar. Geol.* **192** (1), 105–121.

KUENEN, P. H. & MIGLIORINI, C. I. 1950 Turbidity currents as a cause of graded bedding. *J. Geol.* **58**, 91–127.

LESSHAFFT, L., HALL, B., MEIBURG, E. & KNELLER, B. 2011 Deep-water sediment wave formation: linear stability analysis of coupled flow/bed interaction. *J. Fluid Mech.* **680** (1), 435–458.

LIN, Q., LINDBERG, W. R., BOYER, D. L. & FERNANDO, H. J. S. 1992 Stratified flow past a sphere. *J. Fluid Mech.* **240** (1), 315–354.

LUTHI, S. 1981 Experiments on non-channelized turbidity currents and their deposits. *Mar. Geol.* **40** (3–4), 59–68.

MASON, P. J. & MORTON, B. R. 1987 Trailing vortices in the wakes of surface-mounted obstacles. *J. Fluid Mech.* **175** (1), 247–293.

MASON, P. J. & SYKES, R. I. 1979 Three-dimensional numerical integrations of the Navier–Stokes equations for flow over surface-mounted obstacles. *J. Fluid Mech.* **91**, 433–450.

MEIBURG, E. & KNELLER, B. 2010 Turbidity currents and their deposits. *Annu. Rev. Fluid Mech.* **42** (1), 135–156.

MIDDLETON, G. V. 1993 Sediment deposition from turbidity currents. *Annu. Rev. Earth Planet. Sci.* **21** (1), 89–114.

MIGEON, S., SAVOYE, B., ZANELLA, E., MULDER, T., FAUGÈRES, J. C. & WEBER, O. 2001 Detailed seismic-reflection and sedimentary study of turbidite sediment waves on the Var Sedimentary Ridge (SE France): significance for sediment transport and deposition and for the mechanisms of sediment-wave construction. *Mar. Petrol. Geol.* **18** (2), 179–208.

MITTAL, R., DONG, H., BOZKURTTAS, M., NAJJAR, F. M., VARGAS, A. & VON LOEBBECKE, A. 2008 A versatile sharp interface immersed boundary method for incompressible flows with complex boundaries. *J. Comput. Phys.* **227** (10), 4825–4852.

MOHD-YUSOF, J. 1997 Combined immersed-boundary/B-spline methods for simulations of flow in complex geometries. In *CTR Annual Research Briefs* pp. 317–327. NASA Ames/Stanford University, (1).

NAKAJIMA, T. & SATOH, M. 2001 The formation of large mudwaves by turbidity currents on the levees of the Toyama deep-sea channel, Japan Sea. *Sedimentology* **48** (2), 435–463.

NASR-AZADANI, M. M., HALL, B. & MEIBURG, E. 2013 Polydisperse turbidity currents propagating over complex topography: comparison of experimental and depth-resolved simulation results. *Comput. Geosci.* **53** (0), 141–153.

NASR-AZADANI, M. M. & MEIBURG, E. 2011 TURBINS: an immersed boundary, Navier–Stokes code for the simulation of gravity and turbidity currents interacting with complex topographies. *Comput. Fluids* **45** (1), 14–28.

NASR-AZADANI, M. M. & MEIBURG, E. 2013 Influence of seafloor topography on the depositional behaviour of bi-disperse turbidity currents: a three-dimensional, depth-resolved numerical investigation. *Environ. Fluid Mech.* doi: 10.1007/s10652–013-9292-5.

NECKER, F., HÄRTEL, C., KLEISER, L. & MEIBURG, E. 2002 High-resolution simulations of particle-driven gravity currents. *Intl J. Multiphase Flow* **28** (2), 279–300.

NECKER, F., HÄRTEL, C., KLEISER, L. & MEIBURG, E. 2005 Mixing and dissipation in particle-driven gravity currents. *J. Fluid Mech.* **545**, 339–372.

NORMARK, W. R., PIPER, D. J. W., POSAMENTIER, H., PIRMEZ, C. & MIGEON, S. 2002 Variability in form and growth of sediment waves on turbidite channel levees. *Mar. Geol.* **192** (1), 23–58.

NORMARK, W. R., POSAMENTIER, H. & MUTTI, E. 1993 Turbidite systems: state of the art and future directions. *Rev. Geophys.* **31** (2), 91–116.

OEHY, C. D. & SCHLEISS, A. J. 2007 Control of turbidity currents in reservoirs by solid and permeable obstacles. *J. Hydraul. Engng* **133** (6), 637–648.

OOI, S. K., CONSTANTINESCU, G. & WEBER, L. 2009 Numerical simulations of lock-exchange compositional gravity current. *J. Fluid Mech.* **635**, 361.

PEAKALL, J., AMOS, K. J., KEEVIL, G. M., WILLIAM BRADBURY, P. & GUPTA, S. 2007 Flow processes and sedimentation in submarine channel bends. *Mar. Petrol. Geol.* **24** (6), 470–486.

PIRMEZ, C. & IMRAN, J. 2003 Reconstruction of turbidity currents in Amazon channel. *Mar. Petrol. Geol.* **20** (6), 823–849.

ROTTMAN, J. W. & SIMPSON, J. E. 1983 Gravity currents produced by instantaneous releases of a heavy fluid in a rectangular channel. *J. Fluid Mech.* **135** (1), 95–110.

SAU, A., HWANG, R. R., SHEU, T. W. H. & YANG, W. C. 2003 Interaction of trailing vortices in the wake of a wall-mounted rectangular cylinder. *Phys. Rev.* E **68** (5), 056303.

SEQUEIROS, O. E., SPINEWINE, B., BEAUBOUEF, R. T., SUN, T., GARCÍA, M. H. & PARKER, G. 2010 Characteristics of velocity and excess density profiles of saline underflows and turbidity currents flowing over a mobile bed. *J. Hydraul. Engng* **136** (7), 412–433.

SHIN, J. O., DALZIEL, S. B. & LINDEN, P. F. 2004 Gravity currents produced by lock exchange. *J. Fluid Mech.* **521**, 1–34.

SIMPSON, J. E. 1972 Effects of the lower boundary on the head of a gravity current. *J. Fluid Mech.* **53** (04), 759–768.

SIMPSON, J. E. 1997 *Gravity Currents: In the Environment and the Laboratory*. 2nd edn.. Cambridge University Press.

SIMPSON, J. E. & BRITTER, R. E. 1979 The dynamics of the head of a gravity current advancing over a horizontal surface. *J. Fluid Mech.* **94** (3), 477–495.

SMOLARKIEWICZ, P. K. & ROTUNNO, R. 1989 Low froude number flow past three-dimensional obstacles. Part I: baroclinically generated lee vortices. *J. Atmos. Sci.* **46** (8), 1154–1164.

SMOLARKIEWICZ, P. K. & ROTUNNO, R. 1990 Low froude number flow past three-dimensional obstacles. Part II: upwind flow reversal zone. *J. Atmos. Sci.* **47** (12), 1498–1511.

SNYDER, W. H., BRITTER, R. E. & HUNT, J. C. R. 1979 A fluid modelling study of the flow structure and plume impingement on a three dimensional hill in stably stratified flow. In *Wind Engineering-Proceedings of the Fifth International Conference* vol. vol. 1, pp. 319–329. Pergamon Press.

SNYDER, W. H., HUNT, J. C. R., LEE, J. T., CASTRO, I. P., LAWSON, R. E., ESKRIDGE, R. E., THOMPSON, R. S. & OGAWA, Y. 1985 Structure of strongly stratified flow over hills: dividing-streamline concept. *J. Fluid Mech.* **152**, 249–288.

STRAUSS, M. & GLINSKY, M. E. 2012 Turbidity current flow over an erodible obstacle and phases of sediment wave generation. *J. Geophys. Res.* **117** (C6), C06007.

SYVITSKI, J. P., ALEXANDER, C. R., FIELD, M. E., GARDNER, J. V., ORANGE, D. L. & YUN, J. W. 1996 Continental-slope sedimentation: the view from northern California. *Oceanography* **9** (3), 163–167.

TOKYAY, T., CONSTANTINESCU, G. & MEIBURG, E. 2012 Tail structure and bed friction velocity distribution of gravity currents propagating over an array of obstacles. *J. Fluid Mech.* **1** (1), 1–40.

TSENG, Y. H., MENEVEAU, C. & PARLANGE, M. B. 2006 Modelling flow around bluff bodies and predicting urban dispersion using large eddy simulation. *Environ. Sci. Technol.* **40** (8), 2653–2662.

VINOKUR, M. 1983 On one-dimensional stretching functions for finite-difference calculations. *J. Comput. Phys.* **50** (2), 215–234.

VOSPER, S. B., CASTRO, I. P., SNYDER, W. H. & MOBBS, S. D. 1999 Experimental studies of strongly stratified flow past three-dimensional orography. *J. Fluid Mech.* **390**, 223–249.

WINTERS, K. B. & ARMI, L. 2012 Hydraulic control of continuously stratified flow over an obstacle. *J. Fluid Mech.* **700**, 502–513.

WINTERS, K. B., LOMBARD, P. N., RILEY, J. J. & D'ASARO, E. A. 1995 Available potential energy and mixing in density-stratified fluids. *J. Fluid Mech.* **289** (1), 115–128.

WOODS, A. W., BURSIK, M. I. & KURBATOV, A. V. 1998 The interaction of ash flows with ridges. *Bull. Volcanol.* **60** (1), 38–51.

WYNN, R. B. & STOW, D. A. V. 2002 Classification and characterisation of deep-water sediment waves. *Mar. Geol.* **192** (1–3), 7–22.

WYNN, R. B., WEAVER, P. P. E., ERCILLA, G., STOW, D. A. V. & MASSON, D. G. 2000 Sedimentary processes in the Selvage sediment-wave field, NE Atlantic: new insights into the formation of sediment waves by turbidity currents. *Sedimentology* **47** (6), 1181–1197.

XU, J. P., NOBLE, M. A. & ROSENFELD, L. K. 2004 In-situ measurements of velocity structure within turbidity currents. *Geophys. Res. Lett.* **31** (9), L09311.

YALIN, M. S. & KARAHAN, E. 1979 Inception of sediment transport. *J. Hydraul. Div.* **105** (11), 1433–1443.